

Machine Learning Assisted Chemical Characterization and Optical

Properties of Atmospheric Brown Carbon in Nanjing, China

Yu Huang¹, Xingru Li², Dan Dan Huang³, Ruoyuan Lei¹, Binhuang Zhou¹,

Yunjiang Zhang¹, Xinlei Ge^{1, 4*}

¹ Jiangsu Key Laboratory of Atmospheric Environment Monitoring and Pollution Control, Collaborative Innovation Center of Atmospheric Environment and Equipment Technology, School of Environmental Science and Engineering, Nanjing University of Information Science and Technology, Nanjing 210044, China

² Analytical Instrumentation Center, Department of Chemistry, Capital Normal University, Beijing, 100048, China

³ Shanghai Academy of Environmental Sciences, Shanghai 200233, China

⁴ School of Environment and Energy Engineering, Anhui Jianzhu University, Hefei 230601, China

*Corresponding author: Xinlei Ge (Email: caxinra@163.com)

For Atmospheric Chemistry and Physics

Abstract: The light-absorbing organics, namely brown carbon (BrC), can significantly affect atmospheric visibility and radiative forcing, yet their current knowledge of chemical composition of BrC is largely limited to a number of certain classes of compounds; the chemical and optical properties, and particularly linkage between the two remain poorly understood. HereTo address this, a comprehensive analysis was conducted on the particulate matter (PM_{2.5}) samples collected in Nanjing, China during 2022 ~ 2023 with a particular interestfocus on the identification of key BrC molecules. Several important clues related to BrC were found. First, the water-soluble organic aerosol (WSOA) was more oxygenated during cold season (CS) due to a highly oxidized secondary OA (SOA) factor that was strongly associated with aqueous/heterogeneous reactions especially during nighttime, while the WSOA during summer season (SS) was less oxygenated and the SOA was mainly from photochemical reactions. Fossil fuel combustion hydrocarbon-like OA was the largest and dominant contributor to the light absorption during CS (55.6 ~ 63.7%). Secondly, our observations reveals that aqueous oxidation can lead to notable photo-enhancement during CS, while photochemical oxidation on the contrary caused photo-bleaching during SS; Both water-soluble and methanol-soluble organics had four key fluorophores, including three factors relevant with humic-like substances (HULIS) and one protein-like component. Thirdly, molecular characterization show that CHON compounds were overall the most abundant species, followed by CHO and CHN compounds, and significant presence of organosulfates in CS samples reaffirmed the importance of aqueous-phase formation. Finally, building upon the molecular characterization and light absorption measurement results, the machine learning approach was applied to identify the key BrC molecules, and 31 compounds including polycyclic aromatic hydrocarbons (PAHs), oxyheterocyclic PAHs, quinones, and nitrogen-containing species, etc., which can be a good reference for future studies.

1 Introduction

In ambient air, some organic aerosol (OA) species can absorb light in the near-ultraviolet (UV) and visible spectrum, ~~and are~~ termed as “brown carbon (BrC)” (Andreae and Gelencsér, 2006; Chen et al., 2020b). The BrC absorption exhibits strong wavelength-dependence that typically the absorption increases as the wavelength decreases (Laskin et al., 2015). ~~A prior study has reported that BrC is responsible for approximately 40 % of UV-Vis light absorption; it can also contribute to the darkening of ice and snow surfaces, particularly in low-latitude and polar regions (Yan et al., 2018; Brown et al., 2022; Chakrabarty et al., 2023), and thus. Thus,~~ BrC can play a crucial role in global climate and air quality (Jo et al., 2016; Feng et al., 2013). ~~For examples, some~~ Some studies show that the global radiative forcing of BrC ranges from approximately 0.22 to 0.57 W m⁻², equivalent to 27 ~ 70 % of that of black carbon (BC) (Lin et al., 2014; Zhang et al., 2017). ~~Given such importance, recently many researches have been conducted to characterize the optical properties, sources, as well as chemical composition of BrC.~~ Xu et al. (2024) used a global climate model to estimate that BrC accounts for 19% and 12% of the total light absorption by carbonaceous aerosols, with the direct radiative forcing of 0.110 W m⁻² and 0.205 W m⁻² in China during winter and summer, respectively. Delessio et al. (2024) estimated a top-of-the-atmosphere (TOA) radiative effect of BrC to be 0.04 W m⁻².

The sources of atmospheric BrC are highly complex, as it can originate from multiple ~~primary emission~~ sources (Hecobian et al., 2010; Chakrabarty et al., 2010; Gu et al., 2022) as well as various secondary chemical processes (Wang et al., 2021) (Fleming et al., 2020; Jiang et al., 2021; Chen et al., 2020b). The primary sources mainly include coal combustion, biomass burning, and vehicular emissions (Wang et al., 2016; Sun et al., 2016; Qi et al., 2019; Chen et al., 2018; Gu et al., 2022); besides, a significant presence of chromophores originating from the ocean has been observed, indicating that the ocean/marine emission is likely also an important source of BrC (Cavalli et al., 2004). As said, secondary BrC species can be generated from many processes, for instances, the aromatic secondary OA (SOA) species formed under high

NO_x concentrations (Jaoui et al., 2006), reaction products of biogenic or anthropogenic SOAs with nitrogen-containing substances such as NH₃ and NH₄⁺ (Updyke et al., 2012; Shapiro et al., 2009; Bones et al., 2010), and aqueous-phase reaction products from various carbonyl/phenolic precursors in cloud, fog, and aerosol water (Hu et al., 2017; Ye et al., 2018; Wang et al., 2021; Li et al., 2023; Ou et al., 2021).

The ~~light absorption~~optical properties of BrC are ~~also~~ closely related with its ~~sources and composition of OA~~. Recent studies have linked BrC light absorption with its various sources (both primary and secondary) ~~deconvoluted~~resolved from factor analysis of OA data determined by the aerosol mass spectrometry (AMS) (Chen et al., 2020b; Zhong et al., 2023; Chen et al., 2016), and provided the mass absorption efficiency (MAE) of individual BrC source/factor. ~~In addition, the fluorescent properties are also investigated, which identified different types of humic-like substances (HULIS) and protein-like species as the key components (Xie et al., 2020; Chen et al., 2020a; Chen et al., 2021).~~

~~Essentially, the light absorption properties of BrC are governed by its chemical constitution.~~ Current studies have identified several ~~key~~ classes of light-absorbing organics in ~~atmospheric aerosols~~ambient OA, such as ~~the~~ aromatic carboxylic acids, phenols, nitroaromatic compounds (NACs), polycyclic aromatic hydrocarbons (PAHs) and their derivatives (Lin et al., 2018; Huang et al., 2018; Wang et al., 2021; Xing et al., 2023; Gu et al., 2022; Chen et al., 2020b; Kuang et al., 2023; Laskin et al., 2025). Some lignin pyrolysis/burning products including coumarins, flavonoids, stilbenes, and several sulfur-containing species are also ~~found as~~ significant BrC constituents (Fleming et al., 2020; Budisulistiorini et al., 2017; Huang et al., 2022). Xing et al. (2023) identified a series of BrC chromophores, encompassing nitrophenols, benzoic acids, oxygenated PAHs, phenols, aryl amides/amines, phenylpropene derivatives, coumarins and flavonoids, pyridines, and nitrobenzoic acids. ~~Nevertheless, knowledge regarding the molecular composition of BrC so far is still incomplete and the aforementioned identified species only occupy a limited fraction of the BrC total light absorption.~~ Nevertheless, knowledge regarding the molecular composition of BrC so far

域代码已更改

is still incomplete and the identified species only occupy a limited fraction of the BrC total light absorption (<25%) (Wang et al., 2024). For examples, Zhang et al. (2013) measured eight NACs in Los Angeles and found that they contributed about 4 % of water-soluble BrC light absorption at 365 nm; Huang et al. (2018) measured 18 PAHs and their derivatives in Xi'an and found that they accounted for on average ~ 1.7 % of the overall absorption of methanol-soluble BrC; Gu et al. (2022) quantified eight NACs present in PM_{2.5} during winter in Nanjing, which together accounted for at most ~9 % of the total BrC absorption at 365 nm. On the other hand, the fluorescent properties of OA can be determined by the excitation-emission matrix (EEM) fluorescence spectroscopy (Murphy et al., 2013; Stubbins et al., 2014). By performing the parallel factor analysis (PARAFAC) on EEM data, the key fluorophores can be identified (Xie et al., 2020; Chen et al., 2020a; Chen et al., 2021). samples collected during winter in Nanjing, which together could account for at most ~9 % of the total BrC absorption at 365 nm. These fluorophores are also linked with different sources such as biomass burning, coal combustion, and vehicle emissions (Tang et al., 2020).

Emerging non-targeted approaches based on gas chromatography (GC) or liquid chromatography (LC) coupled with high-resolution mass spectrometry can detect hundreds to thousands of molecules in OA (Kuang et al., 2023; Mao et al., 2022), enabling the identification of potential BrC species by connecting them with light absorption of OA. However, these approaches often output high-dimensional data with numerous variables, which must be evaluated appropriately. Traditional statistical methods often perform poorly when handling large datasets and fail to accurately identify complex relationships between interplays among variables (Fasola et al., 2020). Machine learning (ML) is a powerful tool that can effectively recognize and resolve such nonlinear relationships between variables and address issues of collinearity among the variables (Tang et al., 2024). For instances, Zhang et al. (2023) employed the Random Forest (RF) algorithm to quantify the factors driving PM_{2.5} trends in six cities on Tibetan Plateau from 2015 to 2022, revealing the importance of anthropogenic emission reductions; Wang et al. (2022a) integrated the positive matrix

域代码已更改

factorization (PMF) with a multi-layer perceptron (MLP) neural network to analyze the sources of BrC light absorption in six major Chinese cities, which finds that primary emissions, including biomass burning, vehicle emissions, and coal combustion, significantly contribute to BrC in these cities, while secondary processes contributed more significantly to light absorption in southern cities than in northern cities.

employed the Random Forest (RF) algorithm to quantify the factors driving PM_{2.5} trends in Tibetan Plateau from 2015 to 2022, revealing the importance of anthropogenic emission reductions, and a similar ML approach was used for resolving the driving factors of ozone pollution too (Zhu et al., 2024). Li et al. (2022b) applied the ML-RF approach to analyze the sources of OA in submicron PM (PM₁) and PM_{2.5}, showing the importance of secondary processes in supermicron PM. Wang et al. (2022a) integrated the positive matrix factorization (PMF) with a multi-layer perceptron (MLP) neural network to analyze the sources of BrC light absorption. Very recently, Wang et al. (2024) applied the ML method to predict the optical properties of BrC with known chromophores.

In this study, we conducted a systematic investigation on the chemical and optical properties on the fine particular matter (PM_{2.5}) samples in both daytime and nighttime collected in Nanjing, China during summer and cold seasons of 2022 ~ 2023. Particularly, for the first time, we applied the ML-RF algorithm to connect the light-absorbing characteristics with the determined organic ~~molecular identities, molecules,~~ aiming to assist the screen of identify more unknown key BrC molecules. Our findings regarding the BrC properties, ~~and~~ especially the BrC molecules ~~proposed here~~ identified can be a good reference, and the ML application can be an example of practice for future studies— as well.

2 Experimental methods

2.1 Sampling site and sample collection

The PM_{2.5} filter samples were collected in ~~the~~ Nanjing, China, from July 11 to August 23, 2022, November 30 to December 10, 2022, February 13 to February 20,

2023, and March 3 to March 31, 2023. The first period represents the hot summer season (SS) (81 samples), and the later three periods represent the cold season (CS)(83 samples); note samples were not collected during precipitation ~~events~~ in both seasons. The sampling site was located inside the campus of Nanjing University of Information Science and Technology (32°12'20.82"N, 118°42'25.46"E). The site was in a suburban area, surrounded by residential buildings, ~~and~~ close to traffic arteries, and industrial zones (including chemical engineering ~~and~~ petrochemical ~~plants~~, power plants and ironmaking and steelmaking plants).

A high volume sampler (Jinshida Ltd. Qingdao, China, model KB-1000) with a flow rate of 1.05 m³ min⁻¹ was employed. PM_{2.5} samples were collected on the prebaked (450 °C) quartz fiber filters (Pallflex, USA, size of 8 × 10 inch). Daytime samples were collected from 08:00 to 18:00 (Local Beijing time), and nighttime samples were collected from 19:00 to 07:00 on the next day. Each filter was wrapped in an aluminum foil and kept frozen at -20 °C until analysis. The concentrations of common gas pollutants (SO₂, NO₂, CO, and O₃) were obtained from the nearby National Environmental Monitoring Center (<http://www.cnemc.cn/>), while the meteorological parameters (air temperature, relative humidity, wind speed and direction) were recorded in the same site as PM_{2.5}.

2.2 Chemical analyses

2.2.1 Measurements of inorganic ions, organic carbon (OC) and elemental carbon (EC)

A number of round pieces (20 mm diameter) were punched from each sample filter, and were extracted by using 50 mL of ultrapure water (18.25 MΩ cm) (10 pieces) and methanol (4 pieces), respectively. The filter pieces underwent 30 minutes of sonication and were filtrated through the polytetrafluoroethylene (PTFE) syringe filters (0.22 μm) to remove insoluble materials. Cations (NH₄⁺, Na⁺, K⁺, Mg²⁺, Ca²⁺) were measured using a 881 Compact IC ~~pro-ion-chromatographyPro~~ (Metrohm, Switzerland), anions (NO₃⁻, SO₄²⁻, Cl⁻, F⁻) ~~arewere~~ determined by the ICS2100 (Dionex, USA). The water-

soluble organic carbon (WSOC) ($\mu\text{g C m}^{-3}$) was measured by a total organic carbon (TOC) analyzer (TOC-L, Shimadzu, Japan). Operational details of these analyses can be found in our previous work (Chen et al., 2020a).

Concentrations of total elemental carbon (EC) and organic carbon (OC) in samples were measured using a thermal optical carbon analyzer (RT-4; Sunset Laboratory, USA) on a separate round filter piece (17 mm diameter) by using the IMPROVE TOT protocol (Bai et al., 2020). In addition, the residual OC and EC contents in samples after methanol extraction were determined with the same method ~~mentioned~~ above, and were subtracted from the total OC content, to derive the methanol-soluble OC (MSOC) ($\mu\text{g C m}^{-3}$).

2.2.2 Bulk analysis of organics

We employed specially an Aerodyne soot particle AMS (SP-AMS) to determine the bulk composition of water-soluble OA (WSOA) (Onasch et al., 2012). It should be noted that, direct AMS analysis on the methanol-soluble OA (MSOA) is currently unfeasible, even though it might be more important than WSOA in both concentration and light absorption. Likewise almost all offline AMS analysis methods (O'brien et al., 2019; Vasilakopoulou et al., 2023), this is due to that the methanol solvent and its associated organic impurities cannot be effectively removed, making the obtained MSOA signals unidentifiable.

The analysis procedure of WSOA is similar to that described in Ge et al. (2017). In brief, eight round pieces (20 mm diameter) of each filter were sonicated in 40 mL of ultrapure water, and the aqueous extract was nebulized using an atomizer (TSI, Model 3076), then the mist was dried by a silica gel diffusion dryer and the remaining particles were sent to the SP-AMS. The SP-AMS was operated in a laser-off mode, therefore ~~to~~ measure it measured non-refractory species that can be rapidly vaporized at 600 °C (SP-AMS oven temperature). Note the SP-AMS employs a 70 eV electron impact (EI) ionization scheme, ~~therefore so~~ the vaporized species are fragmented into positively charged ions with ~~specified~~ different mass-to-charge (m/z) ratios and we obtained the composition of WSOA in the form of lumped molecular fragments rather than detailed

molecular composition.

The SP-AMS data were post-processed using the Igor-based ToF-AMS analysis toolkit (SQUIRREL version 1.56D and PIKA version 1.15D⁷⁷). Elemental ratios including hydrogen-to-carbon (H/C), oxygen-to-carbon (O/C) and nitrogen-to-carbon (N/C) as well as the organic mass to organic carbon (OM/OC) ratio were calculated by using the methods proposed in Aiken et al. (2008), Canagaratna et al. (2015) and Ge et al. (2024). The WSOA mass concentration of each sample was normalized by multiplying the WSOC concentration with its corresponding OM/OC. Then, we conducted the PMF analysis to resolve the sources of WSOA by utilizing the PMF evaluation toolkit (Version 2.06) (Ulbrich et al., 2009), followed strictly the protocol described in Zhang et al. (2011). As usual, we included only ions with $m/z \leq 120$, and PMF solutions were explored by varying the number of factors (from 3 to 8) and the rotation ~~parameter~~^{parameters} (f_{peak} , from -1 to 1 with an increment of 0.2). Based on the diagnostic plots in Fig. S1 in the supplement, the four-factor solution was selected as the best solution. The ~~four~~ factors include a hydrocarbon-like OA (HOA) relevant with fossil fuel combustion, a biomass burning-related OA (BBOA), a less oxidized oxygenated OA (OOA1) and a more oxidized oxygenated OA (OOA2) (see details in Sect. 3.1.2).

2.2.3 Molecular characterization of organics

Molecular-level characterization of organic species was conducted by using an ultra-high performance liquid chromatography with a quadrupole time-of-flight (QTOF) mass spectrometer (UPLC-QTOF-MS) (ACQUITY UPLC H-Class coupled with a Xevo G2-XS QTOF, Waters). The sample pretreatment was described in Text S1⁷⁸, and the analyzed organics are those dissolved in methanol (namely MSOA). Compound separation was performed with a Luna Omega 1.6 μm C18 column (100 mm \times 2.1 mm \times 1.6 μm), and the sample aliquot was subjected to electrospray ionization (ESI), and detected in both positive and negative ion modes. The scanning m/z range for each mass spectrum was 50-1200, with a scanning rate of one spectrum per 0.1 second. More details are presented in Text S2.

The original UPLC-QTOF-MS data were processed using the Mass Spectrometry-Data Independent Analysis (MS-DIAL, version 4.92) software (Tsugawa et al., 2015), including peak extraction, alignment and deconvolution, achieving a detection probability of 70% in all samples for any identified compound. The method of systematic error removal using random forest (SERRF, a ML algorithm), was then introduced to reduce systematic errors and normalize the measured data (Fig. S2). All deconvoluted spectra were imported into the SIRIUS (Version 5.6.2) toolkit (Dührkop et al., 2019) to determine molecular formulas. The semi-quantitative concentrations of identified molecules were expressed in the normalized peak areas (NPRs), defined as their peak areas acquired from SERRF divided by air volumes of the samples.

In addition, the double-bond equivalent (DBE) was used to indicate the level of unsaturation of the compound (Bae et al., 2011), and the aromaticity equivalent (Xc) (Yassine et al., 2014) was used to indicate the molecular structure. O/C, H/C and DBE values of the sample were averaged over all identified molecules based on their relative abundances (See details in Text S3).

2.3 Optical analyses

2.3.1 Light absorption properties

The light absorption spectra of both WSOC and MSOC in 200 ~ 800 nm were obtained using a UV-Vis spectrophotometer (UV-3600, Shimadzu, Japan) with a 0.5 nm interval. The absorbance at a certain wavelength λ (A_λ) were corrected by subtracting that at 700 nm (A_{700}) (near zero, as background), and the corresponding light absorption coefficient (Abs_λ , $M\ m^{-1}$) is calculated as below (Hecobian et al., 2010):

$$Abs_\lambda = (A_\lambda - A_{700}) \times \frac{V_l}{V_a \times L} \times \ln(10) \quad (1)$$

Where V_l represents volume of the extract (water or methanol), V_a denotes air volume of the filter piece, and L is the optical path length (0.01 meters here).

The corresponding mass absorption efficiency (MAE_λ , $m^2\ g^{-1}$) can then be calculated below:

$$MAE_\lambda = \frac{Abs_\lambda}{[WSOC] - [MSOC]} \quad (2)$$

Where [WSOC] ([MSOC]) represents the mass concentration of WSOC (MSOC). Following previous studies (Laskin et al., 2015; Chen et al., 2018; Xie et al., 2020; Chen et al., 2020b), the light absorption at 365 nm (Abs_{365}) was employed as a surrogate for BrC in this work.

The relationship between the Absorption Ångström Exponent (AAE)(an index of the wavelength dependence) (Andreae and Gelencsér, 2006) and light absorption is shown below:

$$Abs_{\lambda} = K \cdot \lambda^{-AAE} \quad (3)$$

Where K is a constant related to light absorption, and we computed the AAE values in the 300 ~ 450 nm range.

Additionally, a multi-linear regression (MLR) method was used to estimate the contributions of different WSOA factors to the light absorption of total WSOA, as shown in the following equation :

$$Abs_{365,WSOC} = a \times HOA + b \times BBOA + c \times OOA1 + d \times OOA2 \quad (4)$$

Here, HOA, BBOA, OOA1, and OOA2 represent time series of the WSOA factors. a , b , c , and d are the fitting parameters, which are the mass absorption efficiency (MAE) values of corresponding factor.

The direct radiative forcing effect of BrC can be represented by the simple forcing efficiency (SFE) (in $W\ g^{-1}$), which is the energy added to the earth-atmosphere system per unit mass of aerosol (Bond and Bergstrom, 2006). The SFE of BrC at the wavelength λ can be expressed below (Chen and Bond, 2010):

$$\frac{dSFE}{d\lambda} = -\frac{1}{4} \frac{dS(\lambda)}{d\lambda} \tau_{atm}^2(\lambda)(1-F_C) [2 \times (1-\alpha_s)^2 \beta(\lambda)MSE(\lambda) - 4 \times \alpha_s \times MAE(\lambda)]d\lambda \quad (4)$$

$$\frac{dSFE}{d\lambda} = -\frac{1}{4} \frac{dS(\lambda)}{d\lambda} \tau_{atm}^2(\lambda)(1-F_C) [2 \times (1-\alpha_s)^2 \beta(\lambda)MSE(\lambda) - 4 \times \alpha_s \times MAE(\lambda)]d\lambda \quad (5)$$

Where $S(\lambda)$ represents the solar irradiance at λ obtained from the ASTM G173-03 reference spectra. τ_{atm} denotes the atmospheric transmission (0.79), F_C is set to 0.6, indicating the fraction of cloud cover, the global average value of α_s is fixed at 0.19, representing the surface albedo, β is the backscatter fraction, and MSE and MAE are

the mass scattering efficiency and mass absorption efficiency of BrC, respectively. .

When estimating the radiative effect of BrC, the direct radiative forcing caused by aerosol scattering can be neglected. Therefore, the absorbed radiative forcing within a given spectral range is calculated by the simplified Eq. (56):

$$SFE = \int \frac{dS(\lambda)}{d\lambda} \tau_{atm}^2(\lambda)(1 - F_c) \times \alpha_s \times MAE(\lambda) d\lambda \quad (5)$$

$$SFE = \int \frac{dS(\lambda)}{d\lambda} \tau_{atm}^2(\lambda)(1 - F_c) \times \alpha_s \times MAE(\lambda) d\lambda \quad (6)$$

2.3.2 Fluorescence properties

Characterization of excitation-emission matrix (EEM) of the extracts was performed using a fluorescence spectrophotometer (Cary Eclipse, Agilent, USA). The wavelength range of excitation was set from 230 to 500 nm, and that of emission was from 250 to 600 nm, the scanning resolutions of excitation and emission were 5 nm and 2 nm, respectively, with the scanning speed of 1200 nm min⁻¹. The photomultiplier tube (PMT) detector voltage was set at 600 V. The measurement was subjected to instrument calibration, internal filter correction, Raman/Rayleigh scattering correction, and all EEM spectra were subjected to blank filter subtraction. The processed data were further analyzed using ~~the parallel factor analysis~~ (PARAFAC) to group potential components with similar fluorescent properties. The analysis was performed using MATLAB 2022b software with the drEEM toolbox (Murphy et al., 2013).

Fluorescent properties of the extracts were also characterized by the humification index (HIX), biological index (BIX), and fluorescence index (FI). HIX is defined as the ratio of integrated fluorescence emission intensity in the range of 435 - 480 nm to that in the range of 300 to 345 nm when excited at 254 nm; BIX is calculated as the ratio of emission intensity at 380 nm to that of 430 nm for the excitation wavelength of 310 nm; FI is the ratio of emission intensity at 470 nm to that of 520 nm under a fixed 370 nm excitation wavelength (Birdwell and Engel, 2010; Mcknight et al., 2001).

2.4 Machine learning ~~screening~~identification of key light-absorbing species

The ML RF model was used here to screen the key light absorbing species by linking the target variable (Abs₃₆₅) with the identified organic molecules (in NPRs), via

the “randomforest()” function in R software (Version 4.3.2). Note both light absorption and organic molecules are for MSOA. The model included 500 decision trees and estimated the variance through a cross-validation during training. The dataset was divided into a training set (80% of total) and a test set (20% of total) to assure accuracy and robustness of the model.

The model outputted two key indices to assess the importance of each molecule to the light absorption. One metric is IncNPu_val, which can measure the purity of nodes. During the construction of each tree in the RF model, each split can increase the purity of nodes, therefore if more frequently a variable is used in splitting, more contribution it has to the increase of purity of nodes, then the variable is considered to be important. IncMSE_val is another index based on the mean squared error (MSE). When we permute a variable, increase in the projected error can serve as a measure of its importance. If a variable with a significant impact on the predicted results is permuted, the model's MSE would increase significantly, resulting in a high IncMSE_val value (González et al., 2015). Under the 50th percentile of IncMSE_val, some variables had zero or even negative contributions to IncMSE_val. Considering the definition of IncMSE_val, such variables would have either no or negative influence on model fitting, thus only the top 50 % of compounds were chosen. Afterwards, intersection of the two indices were considered as potential BrC chromophores.

Moreover, a molecule typically requires a substantial uninterrupted conjugation on its molecular backbone to effectively absorb visible light (Lin et al., 2018), therefore a compound with the ratio of DBE to carbon (DBE/C) greater than that of linear polyenes (with a molecular formula of C_xH_{x+2} , $DBE/C = 0.5$) (Cain et al., 2014) is treated as a potential BrC compound. Besides, the DBE/C ratio should be less than the upper limit of DBE for natural compounds ($DBE/C = 0.9$) (Lobodin et al., 2012). Finally, the candidate compounds passed aforementioned procedurescriteria were compared with those in open-source databases, including MoNA (<https://mona.fiehnlab.ucdavis.edu/>) and MassBankEU (<https://massbank.eu/>), to be interpreted as the key BrC compounds.

3 Results and discussion

3.1 Chemical properties

3.1.1 General characteristics

During the sampling period, the temperatures were 34.34 ± 3.23 °C (daytime) (\pm one standard deviation, hereinafter) and 30.85 ± 2.97 °C (nighttime) during SS, 13.00 ± 6.04 °C (daytime) and 9.97 ± 5.04 °C (nighttime) during CS, and the relative humidity (RH) levels were 53.61 ± 10.33 % (daytime) and 65.88 ± 9.87 % (nighttime) during SS, 47.81 ± 18.94 % (daytime) and 55.56 ± 15.74 % (nighttime) during CS, respectively (Figs. 1a and b). Figure 1c depicts the temporal variations of different components. Average concentrations of OC, EC, WSOC, MSOC and total ionic species during daytime and nighttime in the two seasons are summarized in Table 1. Clearly, concentrations of all components were higher in CS than those in SS, but the daytime/nighttime differences were relatively small in both seasons. Also, the MSOC levels were larger than WSOC in all samples. MSOC occupied 82.4 % and 81.5 % while WSOC occupied 61.3 % and 49.5 % of the total OC during SS and CS, respectively, indicating that methanol can more effectively extract the aerosol organics than water.

The mean mass contributions of different ions to their total during SS and CS, respectively are shown in Fig. 1c too. The particles were overall neutral as the molar ratios of inorganic anions to cations were 0.97 and 0.98 during SS and CS, respectively (Fig. S3). The most abundant ion was sulfate in SS (45.5 %) and nitrate in CS (50.7 %), as low temperatures during CS favor the partitioning of nitrate to particle phase. As so, the sulfur oxidation ratio (SOR, $[\text{SO}_4^{2-}]/([\text{SO}_4^{2-}]+[\text{SO}_2])$) and nitrogen oxidation ratio (NOR, $[\text{NO}_3^-]/([\text{NO}_3^-]+[\text{NO}_2])$) were 0.58 and 0.16 (daytime) and 0.56, 0.17 (nighttime) during SS, 0.40, 0.28 (daytime) and 0.42, 0.30 (nighttime) during CS, respectively. NOR was indeed much higher in CS especially during nighttime than those in SS. Furthermore, ammonium (NH_4^+) was the predominant cation while sulfate, nitrate and chloride were major anions. The scatter plots of molar concentrations of ammonium versus summed sulfate, nitrate and chloride (Fig. S4) reveal different bonding forms of the aerosol inorganic salts in different seasons. The correlations were both tight

(correlation coefficients close to 1) yet the fitted slopes during SS were 0.80 (daytime) and 0.89 (nighttime) while those during CS were 0.98 (daytime) and 0.99 (nighttime), respectively. Such results demonstrate that ammonium was deficit to neutralize the cations therefore significant amounts of metal salts (such as sodium/calcium sulfate/nitrate) could exist during SS while during CS, most inorganic species were in the forms of $(\text{NH}_4)_2\text{SO}_4$, NH_4NO_3 and NH_4Cl with no appreciable metal salts.

3.1.2 Features and sources of water-soluble organics

Regarding the water-soluble portion of organic species (WSOA), Figure 2a presents the average high resolution mass spectra (HRMS) during SS and CS, respectively. It can be seen that, WSOA during CS appeared to be much more oxygenated than that during SS (O/C: 0.58, 0.59 vs. 0.44, 0.45). To further unravel causes of such differences, PMF analysis were conducted and the HRMS of resolved factors are presented in Fig. 2b, while mass contributions of these factors during SS and CS as well as the Pearson's correlation coefficients (r) of these factors with other components are illustrated in Fig. 3.

The HOA MS was dominated by C_xH_y^+ ions (57.2 %), such as C_4H_7^+ (m/z 55) and C_4H_9^+ (m/z 57), primarily originating from hydrocarbons emitted from fossil fuel combustion (such as traffic) (Canagaratna et al., 2004). Among the four factors, HOA exhibited the lowest O/C ratio (0.24) and the highest H/C ratio (1.66). This is consistent with the behaviors of HOA from a number of previous offline AMS studies (Daellenbach et al., 2017; Liu et al., 2021; Ye et al., 2017; Qiu et al., 2019). The second factor was identified as BBOA, since it has distinct peaks at m/z 60 (mainly $\text{C}_2\text{H}_4\text{O}_2^+$, 0.76 % of the total ~~MSHRMS~~) and m/z 73 (mainly $\text{C}_3\text{H}_5\text{O}_2^+$, 1.09 % of the total ~~MSHRMS~~), which are characteristic fragments associated with levoglucosan, a tracer compound of biomass burning particles (Kumar et al., 2022; Qin et al., 2017). Correlations between BBOA and these two tracer ions were indeed tight (0.71 with $\text{C}_2\text{H}_4\text{O}_2^+$ and 0.82 with $\text{C}_3\text{H}_5\text{O}_2^+$). A notably positive correlation between BBOA and K^+ (Fig. 3b) further supports its BB origin as K^+ is also a common BB emission tracer (Yu et al., 2018). Note the BBOA here had a relatively higher O/C ratio of 0.61 than those

identified in previous offline AMS measurements, such as Yangzhou (0.45) (Ge et al., 2017), Beijing, China (0.59) (Qiu et al., 2019), and Marseille, France (0.54) (Bozzetti et al., 2017), suggesting the ~~potential~~ presence of partially aged BBOA ~~components~~ species in this factor.

The other two factors are secondary. OOA1 was less oxidized with a O/C of 0.39 and OOA2 was more oxygenated with the highest O/C of 0.65 among all factors. OOA1 had characteristic fragments at m/z 29 (CHO^+) and m/z 43 (mainly $\text{C}_2\text{H}_3\text{O}^+$) while OOA2 had the least fraction of oxygen-free C_xH_y^+ ions (28.5 %) but the largest fraction of oxygenated ions (32.8 % of $\text{C}_x\text{H}_y\text{O}_1^+$ and 18.9 % of $\text{C}_x\text{H}_y\text{O}_2^+$) among the four factors. OOA2 ~~also~~ correlated well with CO_2^+ (m/z 44) ~~ion~~ (r of 0.81), a characterisitic ion of highly oxygenated carboxylic/dicarboxylic acids. Moreover, OOA2 had the highest N/C of 0.095 as well as those of $\text{C}_x\text{H}_y\text{N}^+$ (9.1 %) (such as CH_2N^+ , CHN^+ and CH_4N^+) and $\text{C}_x\text{H}_y\text{O}_2\text{N}^+$ (3.8 %) (such as CHON^+ , CH_2NO^+ and CH_4NO^+) ~~ions~~, indicating the presence of amines and amino acids correspondingly (Ge et al., 2024). Besides, the N/C level of OOA2 is close to that of fogwater observed in Fresno, indicating the aqueous phase reactions are likely an source of those nitrogen-containing ions in OOA2 (Kim et al., 2019). In addition, sulfur-containing organic ions (such as CH_2S^+ , CH_3SO_2^+ and CHS^+) were almost exclusively present in OOA2 and in a significant fraction (2.7 %), as such ions were strongly associated with aqueous/heterogenous reactions (Zorn et al., 2008; Huang et al., 2020; Petters et al., 2021; McNeill, 2015), reassuring that OOA2 was ~~probably~~ very likely linked with aqueous/heterogenous formation pathway.

The time series of mass contributions of the four ~~PMF~~ factors are shown in Fig. 1d, and significant differences can be observed during the two sampling seasons, as can be seen clearly in Fig. 3a. HOA was a significant source in both SS and CS, and as expected, it was higher during daytime due to the stronger traffic activities. BBOA was much less important than HOA, but its contribution during CS was obviously more than that during SS (12.5 ~ 13.0 % vs. 7.2 ~ 7.8 %), and accordingly, HOA contribution was slightly larger during SS than during CS (38.0 ~ 41.7 % vs. 29.9 ~ 36.8 %). ~~The most striking difference lies in two SOA factors. It is worthy to mention that, BBOA can be~~

more important than HOA, such as in Beijing during autumn polluted period (38.3% of WSOA) (Hu et al., 2020), in Delhi, India (31-34% of WSOA) (Bhowmik et al., 2024), and in urban and rural Catalonia, Spain (up to 26% of WSOA) (Veld et al., 2023). In general, the dominance of SOA in WSOA observed here was consistent with most offline AMS studies aforementioned, except that POA was found to dominate WSOA in Delhi, India (Bhowmik et al., 2024). However, mass contributions of the two individual SOA factors in different seasons in this study were strikingly different. OOA1 occupied nearly half of the total WSOA (47.5 ~ 49.8 %) while contributions of OOA2 were only 3.0 ~ 5.0 % during SS; on the other hand, OOA2 occupied 38.6 ~ 43.5 % of WSOA mass while those of OOA1 were down to 11.6 ~ 14.1 %. The much larger OOA2 fraction during CS explains its overall high oxidation degree depicted in Fig. 2. These results are well consistent with our previous studies, as we show that during summer in Nanjing, photochemical reactions dominate the SOA formation and yield relatively less oxygenated OA (Xian et al., 2023; Wang et al., 2022b), while during cold seasons, aqueous formation of SOA becomes more important which can generate highly oxygenated OA (Wu et al., 2021; Wu et al., 2018). The air temperature (a solar radiation indicator) and ozone (a photochemical product) both correlated positively with OOA1 but negatively with OOA2 (Fig. 3b), further verifying the dominance of photochemical pathway production of OOA1 not OOA2. As is well known, particulate nitrate was strongly associated with heterogenous reactions and gas-to-particle partitioning favored by low temperature and high RH especially during CS, and indeed, OOA2 correlated much tighter with NH_4NO_3 than OOA1 did.

3.2 Optical properties

3.2.1 Light-absorbing properties of WSOC and MSOC

The average light absorption coefficients of BrC in WSOC and MSOC in 300 ~ 700 nm during daytime and nighttime of SS and CS are illustrated in Fig. 4a. As expected, the values all exponentially decreased as a function of wavelength. The calculated AAE values are listed in Table 1. It is interesting to find that the WSOC AAE

had no significant difference between SS and CS (6.35 vs. 6.43), while that of MSOC AAE appeared to be notable (5.99 vs. 6.89); Compared with the MSOC AAE, the WSOC AAE was higher during SS but smaller during CS. The AAE values obtained here are slightly smaller than those reported in Beijing (7.3 ~ 7.5 of WSOC) (Du et al., 2014; Chen et al., 2016), comparable to that in Guangzhou (6.7 of WSOC) (Fan et al., 2016). Note Chen and Bond (2010) reports that particles generated from smoldering of various types of wood exhibit a AAE of 6.9 ~ 11.6 (MSOC); Lambe et al.(2013) shows that lab-generated secondary BrC possesses a AAE of 5.2 ~ 8.8 (MSOC). Compared with these values, our measured AAE values (<7) here probably suggest a dominance of secondarily formed BrC for both WSOC and MSOC. This can be verified by Fig. 3a for WSOC, as indeed it was dominated by SOA particularly during nighttime in both seasons. However, the large difference in WSOA chemical composition in different seasons (especially SOA proportions) did not result in a large difference in WSOC AAE, demonstrating clearly the non-correspondence of chemical species to light-absorbing species (a.k.a., BrC). On the contrary, for MSOC, the relatively large difference of MSOC AAE in different seasons likely reflect the distinction of BrC species but not necessarily chemical constitution. The light absorption coefficients at 365 nm (Abs_{365}) are listed in Table 1 too. The average $Abs_{365, WSOC}$ during CS ($4.87 M m^{-1}$) was approximately 2.15 times that of SS ($2.27 M m^{-1}$), and that of MSOC during CS ($4.97 M m^{-1}$) was also much larger than that during SS ($3.64 M m^{-1}$); Nighttime values were higher than those in daytime expect for WSOC during CS. For the same set of samples, $Abs_{365, MSOC}$ values were typically larger than $Abs_{365, WSOC}$ except that CS daytime $Abs_{365, MSOC}$ was slightly smaller than $Abs_{365, WSOC}$ (4.65 vs. $4.89 M m^{-1}$). Scatter plots of Abs_{365} versus WSOC (and MSOC), and $Abs_{365, WSOC}$ versus $Abs_{365, MSOC}$ for the four series of samples are given in Fig. S5. The correlations were generally well especially those of WSOC and MSOC ($r > 0.80$), suggesting that there is a large overlap of extracted species between WSOC and MSOC, as well as their BrC constituents.

Regarding the MAE at 365 nm (MAE_{365}), $MAE_{365, WSOC}$ during CS ($0.75 m^2 g^{-1}$) was higher than that during SS ($0.55 m^2 g^{-1}$), indicating its stronger light absorption

ability during CS; however, the $MAE_{365, MSOC}$, unlike $Abs_{365, MSOC}$, was smaller during CS than that during SS (0.50 vs. $0.72 \text{ m}^2 \text{ g}^{-1}$). Besides, MAE_{365} values for both WSOC and MSOC were slightly larger during nighttime than those during daytime in both seasons. Compared to previous winter studies, the $MAE_{365, WSOC}$ in Nanjing here was lower than that in Beijing ($1.21 \sim 1.26 \text{ m}^2 \text{ g}^{-1}$) (Du et al., 2014; Chen et al., 2016; Li et al., 2020), similar to our earlier observation in Yangzhou ($0.75 \text{ m}^2 \text{ g}^{-1}$), but the $MAE_{365, MSOC}$ appears to be less than that in Yangzhou ($1.12 \text{ m}^2 \text{ g}^{-1}$) (Chen et al., 2020). To further explain the low MAE_{365} observed here, we investigated the air mass origins of our samples collected in different periods via back trajectory analysis (at an altitude of 200 m and 24 hours backwards) using the MeteInfo (Version: 3.0.0) (Wang, 2019). As shown in Fig. S6, only a limited fraction of air mass trajectories passed through sea and coastal areas (clusters 4 and 5, 27.05 % during daytime and 29.54 % during nighttime) during SS, while during CS, proportions of trajectories that intercepted sea/coastal air increased to 79.80 % (clusters 1, 2 and 3 during daytime) and 69.44% (clusters 2, 3 and 4 during nighttime), respectively. Note the air masses during CS are somewhat unusual as typically they mainly originate from inland regions (Wu et al., 2019b), which might cause the low MAE_{365} observed in this work as particles affected by marine air can be less light-absorptive than those influenced by inland air (Li et al., 2022a).

Saleh (2020) proposes a method that uses the MAE_{405} (MAE at 405 nm) – AAE two-dimension space to assess the light-absorbing ability of BrC, as shown in Fig. 4b. The majority of samples in this study fall into the regime of W-BrC (weakly light-absorptive BrC) with a few MSOC samples locating in the VW-BrC (very weak BrC) regime, which are similar to a few other observations (Zhou et al., 2021; Xu et al., 2022). The BrC in MSOC seemed to cover a broader region than it in WSOC, indicating that the MSOC BrC might contain a wider array of species and/or originate from more diverse sources/processes. Daytime/nighttime difference of MSOC BrC was also more obvious than that of WSOC BrC.

At last, we estimated the SFE values of WSOC and MSOC in the range of 300–700 nm, considering the actual visible light wavelength as well as the negligible light

absorption above 700 nm of BrC. As summarized in Table 1, the mean SFE_{MSOC} (2.43 W g^{-1}) during SS was higher than that of WSOC (2.20 W g^{-1}), but it became smaller during CS (2.23 W g^{-1}) and was much lower than that of WSOC (3.24 W g^{-1}). The SFE_{WSOC} values in both SS and CS were lower than that in Beijing ($4.6 \pm 1.7 \text{ W g}^{-1}$ in summer and $6.2 \pm 2.0 \text{ W g}^{-1}$ in winter), especially in CS (Deng et al., 2022). For both WSOC and MSOC, SFE values during nighttime were slightly larger.

3.2.2 Source apportionment of light absorption of WSOC

In Sect. 3.1.2, sources of WSOA were identified and quantified, herein we applied a multiple linear regression (MLR) algorithm to apportion the light absorption of WSOC to these sources. The scatter plot of reconstructed $Abs_{365, WSOC}$ versus measured values are shown in Fig. S7. The fitted slope is 1.06 with a Pearson's r of 0.90, verifying the robustness of this method on our dataset. The calculated regression coefficients, representing the factors' MAE_{365} values ($\text{m}^2 \text{ g}^{-1}$) are listed in Table 2. Compared to our earlier results in Yangzhou (Chen et al., 2020b), the HOA MAE_{365} ($0.71 \text{ m}^2 \text{ g}^{-1}$), was much less than that in Yangzhou ($1.46 \text{ m}^2 \text{ g}^{-1}$), while the BBOA MAE_{365} values were similar (0.71 vs. 0.77); MAE_{365} values of OOA1 ($0.12 \text{ m}^2 \text{ g}^{-1}$) and OOA2 ($0.83 \text{ m}^2 \text{ g}^{-1}$) were very close to the two SOA factors in Yangzhou (0.11 and $0.85 \text{ m}^2 \text{ g}^{-1}$). However, here the less oxygenated OOA1 has the small MAE_{365} while in Yangzhou, the more oxygenated SOA has the similar MAE_{365} as OOA1, and *vice versa* for the other pair. This work finds that the more oxidized SOA has a stronger light absorption ability, opposite to that reported in Yangzhou. Nevertheless, the two findings are not contradictory with each other, as atmospheric ageing can lead to either photo-enhancement or photo-bleachment, dependent upon the precursors. For instances, aqueous oxidation of BBOA can increase (Gilardoni et al., 2016) yet conversely aqueous processing of fossil fuel combustion OA can decrease the light absorptivity of OA (Wang et al., 2021). As discussed in Sect. 3.2.1, the unusual air masses during CS in this work clearly indicate different precursors from those in Yangzhou.

The average contributions of HOA, BBOA, OOA1 and OOA2 to $Abs_{365, WSOC}$ across the whole campaign were 33.05 %, 15.49 %, 6.00 % and 45.46 %, respectively

(Table 2). Figure 5 further presents contributions of the factors under different scenarios. Compared with their mass contributions shown in Fig. 3a, during SS, the dominant contributor of light absorption became HOA (daytime 63.7 %, nighttime 55.6 %), and contributions of BBOA and OOA2 both increased relative to their mass fractions; while OOA1's contribution was largely reduced to 15.0 ~ 16.2 % due to its small MAE₃₆₅. Previous studies have consistently identified coal combustion (Fan et al., 2016; Li et al., 2019; Song et al., 2019) and traffic emissions (Hecobian et al., 2010) as significant contributors to BrC, together with our results here, highlighting the substantial impact of anthropogenic fossil fuel combustion on atmospheric visibility. During CS, OOA2 dominated the light absorption (daytime 50.7 %, nighttime 63.0 %) owing to its large mass contribution as well as large MAE₃₆₅; OOA1 became a very minor contributor (2.1 ~ 2.8 %), HOA contribution decreased while BBOA contribution increased relative to their mass fractions. Overall, we find that primary fossil fuel combustion emissions govern water-soluble BrC light absorption during SS especially during daytime, while during CS, secondary highly aged species (likely from aqueous/heterogenous reactions) dominates, especially during nighttime.

To further explore the impact of atmospheric ageing on BrC, we plotted MAE₃₆₅ as a function of O/C in Fig. 6. Interestingly, during SS, MAE₃₆₅ generally decreased with the increase of O/C, especially in daytime as its fitted slope of -1.56 was over 2 times that of nighttime (-0.76). On the other hand, MAE₃₆₅ showed an increasing trend against O/C during CS, particularly in nighttime as the fitted slope was 1.43, larger than that of daytime (1.12). These results further supports our earlier findings and underscore that during summer photochemical reactions can lead to photo-bleachment of aerosols while during cold seasons aqueous/heterogenous reactions might dominate the secondary formation and lead to photo-enhancement; clearly, photochemical oxidation and aqueous/heterogenous reactions are more active during daytime and nighttime, respectively, consistent with the slopes in Fig. 6. Also, photochemcially produced SOA was often less or moderately oxygenated and that from aqueous/heteregenous oxidation was more oxidized, and there is a turning point at O/C of 0.45 ~ 0.5 in the MAE₃₆₅-O/C

plot, which was found in previous studies too (Zhong et al., 2023; Jiang et al., 2022). Many studies have shown that aqueous reactions are a source of BrC (e.g., Li et al. (2022c), Laskin et al. (2015) and Ye et al. (2019)), but evidence also shows that further aqueous ageing of BrC can lead to photo-bleaching (e.g., Zhao et al. (2015) and Lei et al. (2025)), therefore a certain O/C turning point can exist if the OA evolution was governed by a certain process. The real atmospheric processes are however complicated, such O/C points might be less clear. Nevertheless, similar points were indeed observed previously (Zhong et al., 2023; Jiang et al., 2022).

3.2.3 Fluorescent properties of WSOC and MSOC

The fluorescence indices like HIX, BIX and FI, can infer the types and sources of dissolved organic matter (DOM) in aquatic systems and soils (Lee et al., 2013; Huguet et al., 2009). Recently, these indices have been employed to investigate sources and aging processes of atmospheric OA (Fu et al., 2015; Qin et al., 2018; Deng et al., 2022; Murphy et al., 2013). Here, we calculated these indices for both WSOC and MSOC.

HIX represents the degree of humification, and a high HIX means high aggregation, C/H ratio and aromaticity of the organics (Zsolnay et al., 1999; Mcknight et al., 2001; Birdwell and Engel, 2010), thus it normally increases upon ageing (Fan et al., 2019; Murphy et al., 2013). In this study, HIX of WSOC during SS and CS were on average 3.34 and 4.68, respectively (Table 3), much less than the HIX levels in aquatic or soil DOM (Dong et al., 2017), suggesting an overall low aromaticity of atmospheric OA in Nanjing. As a comparison, the WSOC HIX are higher than those in Colorado, USA (2.42) (Xie et al., 2016) and Tianjin, China (2.73 and 2.22) (Deng et al., 2022), but significantly lower than that in Nanjing during 2017-2018 (7.07) (Xie et al., 2020). An earlier study proposes the HIX ranges of 1.4-5 for fresh SOA and 4.2-6.1 for aged SOA (Lee et al., 2013). Despite influences of other primary sources, the average HIX during SS did fall in the fresh SOA range and the value during CS entered the edge of aged SOA, in line with the oxidation degrees of OA (Fig. 2a) and mass proportions of fresh/aged SOA factors (namely, OOA1/OOA2) (Fig. 3a) during different seasons. The average HIX of MSOC (2.72 and 3.48) were lower than those of WSOC in both seasons,

indicating that HULIS with high aromaticity are preferentially soluble in water.

FI is indicative of the relative contributions of terrestrial and biogenic sources while BIX, in contrast to HIX, can be treated as a freshness index. A fluorophore is often associated with high aromaticity if FI is low (Fu et al., 2015), and a high BIX indicates a high content of freshly released organics (such as biological or microbial derived species) (Wen et al., 2021; Huguet et al., 2009; Murphy et al., 2013). The average WSOC BIX values during SS and CS were determined to be 0.84 and 0.88, respectively, with corresponding FI of 1.91 and 1.90 (Table 3), and the corresponding MSOC BIX were 0.90 and 0.96, and MSOC FI were 2.27 and 2.11, respectively. Compared with results during 2017-2018 in Nanjing, BIX and FI values of WSOC were similar, yet those of MSOC here were larger (Xie et al., 2020). Figure 7 shows the measured data in the HIX-FI and HIX-BIX diagrams along with results from a few other studies. It can be seen that, almost all BIX values distributed in the range of 0.6 ~ 1 (Huguet et al., 2009) and FI values distributed within 1.6 ~ 1.9 (Mcknight et al., 2001), suggesting that OA in both seasons was influenced by a mix of terrestrial and microbial/biogenic sources. For both WSOC and MSOC, BIX was slightly higher during CS than during SS, attributing to the fact that OA during CS contained more aged SOA species. Nearly no difference for WSOC FI during different seasons were observed, but the MSOC FI during CS was slightly lower than that during SS, meaning that MSOC during CS had a high aromaticity as expected. In addition, BIX and FI values during nighttime were marginally higher than those during daytime in all cases.

3.2.4 Identification of key fluorophores of WSOC and MSOC

The 3D EEM-PARAFAC analysis was adopted to identify the key fluorophores of BrC, with results in Fig. 8 and Fig. S8. Four components were resolved for both WSOC and MSOC. For WSOC, C1 exhibited a peak at Ex = 230 nm and Em = 374 nm, identified as less oxidized HULIS typically associated with combustion sources. Its contribution was only 4.9 % during SS but increased to 19.2 % during CS (Fig. S8a). C2 had a prominent peak at Ex = 230 nm and Em = 396 nm and a second peak at Ex = 320 nm and Em = 396 nm, classified as a HULIS-related component too, as the dual-

peak distribution of fluorescence spectrum is often associated with HULIS (Coble, 1996; Murphy et al., 2011; Yu et al., 2015); its second peak indicates the abundance of compounds with condensed aromatics, conjugated bonds, and non-linear rings (Matos et al., 2015), likely a mix of primary and secondary sources. C2 contribution was thus comparable during different seasons (37.5 % vs. 38.6 %), and it seemed to be more important in nighttime than in daytime (44.0 % vs. 26.9 % during SS, and 41.4 % vs. 34.8 % during CS). C3 component, with a peak at Ex = 240 nm and Em = 446 nm, was considered as a highly oxidized ~~HULIS~~HULIS component, relevant with secondary processes (Cheng et al., 2016; Cao et al., 2021). Hawkins et al. (2016) and Aiona et al. (2017) reported fluorescent pattern of products from aqueous-phase reaction of aldehydes with ammonium sulfate or amines (Ex < 250/300 nm and Em > 400 nm) well ~~matches~~matching the pattern identified here. As discussed earlier, aqueous/heterogenous reactions contributed to WSOA, especailly during CS; correspondingly, C3 contribution was indeed much higher during CS than during SS (24.1 % vs. 14.7 %). C4, with a prominent peak at Ex = 230 nm and Em = 308 nm and a second peak at Ex = 275 nm and Em = 305 nm, was characterized as a protein-like component (Yan and Kim, 2017; Wu et al., 2019a; Chen et al., 2020b). C4 was the single largest contributor (42.9 %) during SS particualy during daytime (55.0 %), but became the least ~~one during CS (18.0 %), indicating distinct fluorescent properties of OA in different seasons. Overall, since C1—C3 are all relevant with HULIS, the WSOC fluorescent properties were governed by HULIS (57.1 % in SS and 82.0 % in CS).~~during CS (18.0 %).

Similarly for MSOC, three HULIS-related fluorophores (C1 ~ C3) and one proteinaceous fluorophore (C4) were separated (Fig. 8b). The spectral signatures between the two series of fluorophores were slightly different, with the MSOC peak excitation and emission wavelengths being a bit larger than those of WSOC, especailly for C2 and C3. Figure S8b shows contributions of the different components to MSOC fluorescene. C1 was much more important in MSOC (26.6 % in SS and 39.2 % in CS) than in WSOC, and became the largest contributor of MSOC during CS; summed C2

and C3 contributions (30.7 % in SS and 37.0 % in CS) were on the other hand much less than in WSOC; C4 remained to be the largest (42.6 %) similar to that in WSOC during SS. ~~It is worth to point out that C4 not only contains proteinaceous species like tyrosine and tryptophan but also certain PAHs or phenolic substances emitted from fossil fuel and/or biomass burning, especially in urban aerosols. The increased contributions of the protein-like fluorophore (C4) during SS in both WSOC and MSOC were likely due to its major origin of biological activities, which can be enhanced by the relatively high temperatures during SS (Fan et al., 2020); this is likely the reason that C4 contributions during daytime were higher than those during nighttime in both SS and CS. Furthermore, some studies~~ (Barsotti et al., 2016; Chen et al., 2021; Chen et al., 2020b; Cao et al., 2021; Deng et al., 2022). ~~also point out that C4 not only contains proteinaceous species from biological activities but also certain PAHs or phenolic substances from fossil fuel and/or biomass burning, especially in urban aerosols.~~ Probably, the proteinaceous species dominated the fluorescence during SS for both WSOC and MSOC, while during CS PAHs and phenolic compounds became more important and they might prefer to dissolve in methanol therefore lead to ~~aits~~ higher contribution in MSOC than in WSOC (23.8 % vs. 18.0 %). ~~Daytime/nighttime variations~~ Different solubilities of ~~MSOC were similar~~ HULIS components in water and methanol may partially lead to ~~those of their different contributions in WSOC, as shown in Fig. S8, and MSOC.~~

3.3 Molecular composition of organics

3.3.1 Overview of identified molecules

We classified the identified molecular formulas of organics ~~(here MSOA)~~ via UPLC-QTOF-MS analysis into 8 categories, namely CH, CHO, CHN, CHS, CHON, CHOS, CHNS, and CHONS. Overall, the negative (ESI⁻) and positive (ESI⁺) ion modes identified 466 ~ 865 and 644 ~ 1065 formulas, respectively (details in Table S1). Figures S9 and S10 shows the number and signal fractions (relative abundances of signal intensities) of different classes of compounds, respectively.

Under ESI⁺ mode, CHON compounds were the most abundant species in term of the number fraction – nearly half during SS (daytime 50.5 % and nighttime 46.9 %), and over half during CS (daytime 54.1 % and nighttime 55.1 %), and the abundance of its signal was even more prevailing – over half in all cases and up to 67.7 % during SS daytime; the second abundant species were CHO compounds, occupying 23.0 ~ 30.6 % of the total number of molecules and 15.4 ~ 21.9 % of the total signal intensity; CHONS and CHN species were the other two relatively abundant classes – together occupying ~ 20 % (number fraction) and ~ 10 ~ 24 % (signal fraction) of total identified compounds; contributions of other four classes of compounds were very minor, in terms of both number and signal intensity. Relatively, under ESI⁻ mode, CHO compounds marginally prevailed over CHON compounds in number (36.2 ~ 44.4 % vs. 32.6 ~ 38.0 %), but during CS their signal fractions were still lower (33.3 ~ 35.1 % vs. 39.3 ~ 46.5 %). More enrichment of CHO compounds in ESI⁻ than in ESI⁺ is consistent with a previous work (Lin et al., 2012) as these compounds most likely contain carboxyl groups and are easily deprotonated in ESI⁻ mode. Number fractions of CHONS compounds in ESI⁻ mode were ~5 ~ 10% more than those in ESI⁺ mode, while the most contrasting difference was that CHN compounds were rarely detected in ESI⁺ mode, and instead CHOS compounds that were negligible in ESI⁻ mode could be effectively detected in ESI⁺ mode (3.9 ~ 4.8 % in number) and their signal fractions were more significant (6.4 ~ 17.4 %).

3.3.2 CHO compounds

For the detected CHO compounds, we plotted them in the van Krevelen (VK) diagrams according to their H/C and O/C ratios in Fig. 9. Most molecules had the O/C ratios < 0.5, but a broad distribution of H/C ratios (0.5 ~ 2.0). Molecules with high H/C ratios (≥ 1.5) and low O/C ratios (≤ 0.5) (Region A) were typically associated with aliphatic compounds, while those with low H/C ratios (≤ 1.0) and low O/C ratios (≤ 0.5) (Region B) are usually assigned to oxygenated aromatics (Kourtchev et al., 2014). We further calculated the X_c values of all CHO compounds to investigate their molecular structures in Fig. 9. Clearly, saturated aliphatic CHO compounds (X_c < 2.5) were most

abundant (323 out of 418 in ESI⁺ mode, and 315 out of 481 in ESI⁻ mode) and mainly distributed in Region A. Appreciate number of unsaturated compounds particularly those with benzene ring or naphthalene ring structures ($2.5 < X_c < 2.8$), distributed across from H/C of 0.5 to 1.75 but with O/C < 0.5 in ESI⁻ mode and from H/C of 0.1 to 1.75 but with a few in the side of O/C > 0.5 .

The oxygenation state (OS_c) (Kroll et al., 2011) (defined as $2 \times O/C - H/C$), is another metric to assess the ageing/oxidation degree of a compound. Figure 10 illustrates the dependence of OS_c on carbon number for all CHO compounds. The molecules had a broad coverage of OS_c (-2 to +2) and carbon number (up to 50). Kroll et al. (2011) grouped the compounds into different origins according to their OS_c and C numbers, including fossil fuel combustion HOA, BBOA, semi-volatile oxygenated OA (SV-OOA, typically less-oxidized) and low-volatility oxygenated OA (LV-OOA, typically more-oxidized), as marked in Fig. 10. Obviously, for both ESI⁻ and ESI⁺ modes, a large portion of compounds belonged to HOA and BBOA. In ESI⁺ mode, a significant portion of molecules located in the BBOA region, while in ESI⁻ mode, more molecules tended to be found in the HOA region, and even more molecules located within HOA regime during CS than during SS (Figs. S11 and S12), indicating large influences from anthropogenic emissions. Besides, the number of nighttime LV-OOA molecules was more than that of daytime particular during CS, acting as a supporting evidence of aqueous/heterogeneous reactions.

3.3.3 CHON and CHN compounds

We mapped the detected CHON compounds colored by X_c in the VK diagrams shown in Fig. 11. The compounds were sorted into different series according to the functional groups as well. For ESI⁺ mode (Fig. 11a), the compounds containing a -NO moiety were dominant and a majority of CHON compounds were saturated with $X_c < 2.5$. Among them, $C_6H_{15}NO(CH_2)_n$ might be N,N-diethylethanolamine homologous compounds, and $C_6H_{15}NO_2(CH_2)_n$ might be diisopropanolamine homologous compounds, as both compounds possess lone pair electrons, prone to positive charge (Ge et al., 2011). Unsaturated CHON compounds with $X_c \geq 2.5$ located in the bottom-

left corner, such as $C_5H_5NO(CH_2)_n$, $C_7H_7NO(CH_2)_n$, $C_8H_7NO(CH_2)_n$, and $C_9H_7NO(CH_2)_n$, likely homologous compounds of hydroxypyridine, benzamide, 4hydroxy-benzene acetonitrile, and hydroxyquinoline, respectively (Ma and Hays, 2008; Wang et al., 2020). In ESI⁻ mode, the compounds scattered wider than those in ESI⁺ mode in the VK plot (Fig. 11b), and the majority of them contained one or two nitrogen atoms. Over 25 % of the CHON formulas can be classified as monocyclic or polycyclic compounds with $X_c \geq 2.5$ (even up to 68 % during SS daytime; inferred from Figs. S13 and S14). The identified series of homologous compounds mostly situated in the bottom-left corner and also with $X_c \geq 2.5$, such as $C_6H_5NO_3(CH_2)_n$, $C_6H_5NO_4(CH_2)_n$, $C_8H_7NO_3(CH_2)_n$, $C_8H_7NO_4(CH_2)_n$, and $C_{10}H_7NO_3(CH_2)_n$, likely nitrophenol, nitrocatechol, nitroacetophenone, nitrophenylacetic acid, and nitronaphthol homologues, respectively (Wang et al., 2018b; Song et al., 2019; Lin et al., 2017; Lin et al., 2015).

As stated in Sect. 3.3.1, CHN compounds were only enriched in ESI⁺ mode. The scatter plot of H/C versus N/C of these compounds is depicted in Fig. 12 (results of different periods are shown in Fig. S15). Similarly, they are colored by X_c and sorted into a number of different series. Most of these compounds were amines with one or two N atoms. The series of aliphatic amines and other monocyclic species with $X_c < 2.71$ mostly located in upper part of the plot, including $C_6H_{15}N(CH_2)_n$, $C_5H_{11}N(CH_2)_n$ and $C_6H_{12}N(CH_2)_n$, $C_4H_6N_2(CH_2)_n$, $C_5H_6N_2(CH_2)_n$, $C_7H_6N_2(CH_2)_n$, and $C_{11}H_{17}N(CH_2)_n$. Note the presence of 2 N-heterocyclic species was a sign of presence of BBOA (Wang et al., 2017). The series of $C_{10}H_9N(CH_2)_n$ (1N-PAHs) with $X_c \geq 2.71$ may represent the aminonaphthalene homologues (Ge et al., 2011), likely from initial burning of carbonaceous materials (Mao et al., 2022).

3.3.4 CHOS and CHONS compounds

Among the CHOS formulas (only significant in ESI⁻ mode), ones with O/S ratios ≥ 4 were classified as organosulfates (OSs), which were the most abundant type (Table 4). Its number fractions were particularly high during CS (daytime 54.3 %, nighttime 68.6 %), reiterating the importance of aqueous SOA formation during CS. For the

CHONS compounds, in ESI⁻ mode, 5.3 ~ 12.5 % of the formulas had O/(4S+3N) ratios ≥ 1 , allowing them to be assigned to -OSO₃H and -ONO₂ groups, namely nitrooxy-organosulfates (nitrooxy-OSs) (Wang et al., 2018a); while in ESI⁺ mode, 9.8 ~ 11.8% of total CHONS formulas were apportioned as nitrooxy-OSs (Table 4).

3.4 Machine learning assisted identification of key BrC molecules

~~As stated in Sect. 2.4, the ML-RF algorithm was used to identify the key BrC chromophores, and we finally confirmed 31 compounds (18 in ESI⁺ mode and 13 in ESI⁻ mode);~~To enhance the robustness of ML analysis, we first incorporated all detected compounds without assigned molecular formulas of both positive and negative modes (4953 formulas, ESI⁺: 2863, ESI⁻: 2090) into the ML model. After ML analysis, a total of 1477 molecules (ESI⁺: 795; ESI⁻: 682) were found to have positive values for both IncNPu_val and IncMSE_val. Among them, 1051 molecules (ESI⁺: 420; ESI⁻: 450) were assigned corresponding molecular formulas; and furthermore, a total of 149 compounds with 0.5 < DBE/C < 0.9 (ESI⁺: 52; ESI⁻: 97) were chosen. By comparing with the database, we finally proposed 31 compounds (ESI⁺: 18, ESI⁻: 13) as the key BrC species; details regarding their molecular formulas and proposed structures, etc., are summarized in Table S2. These species are relevant with 4 out of 8 identified types of compounds (CH, CHO, CHN and CHON) (Fig. 13). ~~Note-except~~To the best of our knowledge, 6 out of the 31 species (4-methylcoumarin, urocanate, 3-hydroxybenzoic acid, chrysin, 2-hydroxypyridine and 4-hydroxyacetophenone), ~~all other species were in general) have not been~~ reported as BrC molecules before (See Table S2). ~~as important BrC species.~~

Two PAHs (acenaphthylene and fluoranthene, belonging to CH category) in ESI⁺ mode were identified, ~~which is reasonable as~~consistent with that PAHs are known important BrC (Aurell et al., 2015; Kuang et al., 2021).

Twelve CHO compounds (5 in ESI⁺ mode and 7 in ESI⁻ mode) were identified. In ESI⁺ mode, 9-fluorenone and benzanthrone belonging to oxyheterocyclic PAHs (O-PAHs), are known as important BrC chromophores (Kuang et al., 2023); scopoletin is

also known as a light-absorbing compound (Zhang, 2018); phthalic anhydride is an oxygen-containing heterocyclic compound. A previous study reports that methanol (the solvent used here) might react with conjugated carbonyl species (such as phthalic anhydride, maleic anhydride, and maleimide) (Chen et al., 2022), thereby affecting the light absorption of relevant BrC species, further studies are needed to verify phthalic anhydride as a key chromophore. In ESI⁻ mode, a pair of quinone isomers (1-hydroxyanthraquinone and 2-hydroxyanthraquinone) were resolved, in agreement with Kuang et al. (2023), which identified 1-hydroxyanthraquinone as a BrC chromophore in Beijing; 1-hydroxypyrene is a hydroxylated PAHs, also proven as a BrC before (Huang et al., 2022).

The identified seven CHN compounds (exclusively in ESI⁺ mode) included 4 N-heterocyclics, 2 nitro-PAHs, and 1 quinoline compound. It is well known that biomass burning (BB) release a lot of BrC species. As mentioned earlier, CHN compounds are abundant in BB emissions (such as agricultural waste burning and forest fires (Laskin et al., 2009)); small N-containing heterocyclic compounds with one or two aromatic rings, can be effectively produced from thermal decomposition of plants (Ma and Hays, 2008), and high temperature pyrolysis of CHN compounds and N-containing plant materials, can result in N-PAHs (Lin et al., 2016). Therefore, identification of the CHN species here as key BrC chromophores are well justified.

The remaining confirmed ~~key~~ BrC molecules included 10 CHON compounds (4 in ESI⁺ mode and 6 in ESI⁻ mode). For ESI⁻ mode, 3-hydroxyanthranilic acid is an amino phenolic compound, and the rest five compounds are all nitrophenols, well known as BrC (Li et al., 2020). Another amino phenolic compound, 2-aminophenol was identified in ESI⁺ mode. Previously, efficient light absorption at 275 nm of 2-aminophenol has been reported, which can be further enhanced in the presence of Fe³⁺ due to formation of oligomers (Al-Abadleh et al., 2022). For acridone in ESI⁺ mode, earlier studies have shown that acridine exhibits increased light absorbance in the wavelength range of 260 ~ 320 nm under irradiation in N₂, air, or O₂; additionally, a deep yellow layer forms on the surface, indicating the production of light-absorbing

products, which was identified as acridone (Negron-Encarnacion and Arce, 2007).

For the BrC species identified here, most species contain at least one benzene ring (such as PAHs and NACs) except two compounds (2-hydroxypyridine and urocanate) with other aromatic ring structures. This is reasonable as organic compounds with benzene or other aromatic rings (with conjugated double bonds) are known to be strong light-absorbing. The -OH and -COOH groups on the benzene ring can enhance ultraviolet light absorption at near-UV wavelengths (Jacobson, 1999); The -NO₂ group can further increase light absorbance at longer wavelengths (Jacobson, 1999). Our identified BrC list does include compounds with such functional groups. Note some nitrogen-containing heterocyclic compounds, are usually secondary products of aqueous reactions between carbonyl compounds (such as glyoxal and methylglyoxal) and amines or ammonium (Powelson et al., 2014); thus identification of them here as key BrC species is also a supporting evidence of the occurrence of aqueous reactions.

4 Conclusions

This work performed a comprehensive investigation on the chemical and optical properties of BrC in ambient PM_{2.5} samples. Regarding the chemical properties, it was found that methanol was able to extract more OC than water (~82.0% vs. 49.5 ~ 61.3% of total OC). The WSOA was composed of two primary factors relevant with fossil fuel combustion (HOA) and biomass burning (BBOA), and two SOA factors (a less oxidized OOA1 and a highly oxygenated OOA2). During CS, OOA2 was abundant (38.6 ~ 43.5 %) while during SS OOA1 was abundant (47.5 ~ 49.8 %); HOA was also an important contributor in both seasons (29.9 ~ 41.7%) but BBOA contribution was relatively minor (7.2 ~ 13.0 %). Further analyses reveal that OOA1 was mainly associated with photochemical reactions while OOA2 was strongly linked with aqueous/heterogeneous reactions.—

Regarding the ~~light absorption~~optical properties, our observation shows that Abs_{365, MSOC} was typically larger than Abs_{365, WSOC}, but though MAE_{365, MSOC} was still larger than MAE_{365, WSOC} during SS, it became smaller than the MAE_{365, WSOC} during

CS, likely owing to that the air mass trajectories during CS significantly intercepted sea/coastal air. The light absorbing abilities of both WSOC and MSOC were weak, but our observations suggest that aqueous oxidation can lead to significant photo-enhancement, therefore the light absorption of WSOA was dominated by OOA2 (50.7 ~ 63.0 %) during CS; while photochemical oxidation could cause a photo-bleaching effect and therefore the contribution of OOA1 to WSOA absorbance was small (15.0 ~ 16.2 %), and HOA contribution was prevailing during SS (55.6 ~ 63.7 %). PARAFAC analysis on the fluorescent spectra of WSOC and MSOC both resolved four key components ~~with slightly differences~~, including three HULIS component and one protein-like component. HIX, BIX and FI indices also suggest that both WSOC and MSOC originated from a mix of terrestrial and microbial/biogenic sources.

The molecular analysis determined 644 ~ 1065 molecules in ESI⁺ mode and 466 ~ 865 molecules in ESI⁻ mode. Overall, CHON compounds were the most abundant type especially in ESI⁺ mode, while CHO compounds slightly exceeded CHON compounds in number but were still lower in signal intensity. CHN compounds was the third important class and only detectable in ESI⁺ mode. The VK diagrams further demonstrate the different aromaticity equivalent (Xc) values and evolution pathways of the different classes of compounds. In addition, significant presence of organosulfates and nitroxy-organosulfates in CS samples especially during nighttime re-affirm the importance of aqueous-phase oxidation during CS. ~~At last~~Finally, based on the molecular characterization and light absorption measurement results, we applied the ML RF algorithm to identify the key BrC molecules, and we successfully identified 31 key species, including mainly the PAHs, oxyheterocyclic PAHs (O-PAHs), quinones and N-containing compounds. ~~Overall, our findings presented here expand the scientific understanding regarding the chemical composition; some of them are newly identified.~~

Of course, our study has some limitations. One limitation is that no source apportionment was conducted on MSOA due to technical difficulties, therefore a full closure between emission sources and optical properties of total OA is incomplete;

development of proper method should be the subject of our future work. Moreover, our findings here expand the understanding on chemical (both bulk and molecular level) and optical properties (both light absorption and fluorescence) of BrC, and are valuable to evaluate ~~theirs~~ impact on air quality and radiation balance ~~of BrC. Besides, our, the~~ identified list of key BrC molecules can be a useful reference for future studies. However, our practice with ML approach here serves as only a case study and a valuable attempt, more studies likely with more advanced ML algorithms are needed to identify more BrC species, and to achieve a quantitative closure between the BrC molecules and its total light absorption.

Code availability. The software code to analyze the SP-AMS data is publicly available at: <https://cires1.colorado.edu/jimenez-group/ToFAMSResources/ToFSoftware/index.html>. The software code to analyze the UPLC-QTOF-MS data is publicly available at: <https://systemsomicslab.github.io/compms/msdial/main.html>. The software code using SERRF to normalize UPLC-QTOF-MS data is available at: <https://slfan.shinyapps.io/ShinySERRF/>

Data availability. The data in this study are available from the authors upon request (caxinra@163.com).

Supplement. The supplement related to this article is available online at: XXX

Author contributions. YH, XL and DDH conducted the experiments. YH, XL, RL, BZ, YZ and XG performed the data analysis. YH and XG wrote the paper. All authors reviewed the paper and provide useful suggestions.

Competing interests. The contact author has declared that neither they nor their co-authors have any competing interests.

Disclaimer. Publisher's note: Copernicus Publications remains neutral with regard to jurisdictional claims in published maps and institutional affiliations.

Acknowledgements. We sincerely thank the logistic help from the Center for Experimental Atmospheric Science and Environmental Meteorology of Nanjing University of Information Science and Technology (NUIST) during sampling.

Financial support. This work has been supported by the National Natural Science Foundation of China (grant nos. 22361162668 and 42021004).

Review statement. This paper was edited by XXX, and XXX.

References

Aiken, A. C., DeCarlo, P. F., Kroll, J. H., Worsnop, D. R., Huffman, J. A., Docherty, K. h. S., Ulbrich, I. M., Mohr, C., Kimmel, J. I. R., Sueper, D., Sun, Y. I., Zhang, Q., Trimborn, A., Northway, M., Ziemann, P. J., Canagaratna, M. a. R., Onasch, T. B., Alfarra, M. R., Prevot, A. S. H., Dommen, J., Duplissy, J., Metzger, A., Baltensperger, U., and Jimenez, J. L.: O/C and OM/OC ratios of primary, secondary, and ambient organic aerosols with high-resolution time-of-flight aerosol mass spectrometry, *Environ. Sci. Technol.*, 42, 4478-4485, <https://doi.org/10.1021/es703009q>, 2008.

Aiona, P. K., Lee, H. J., Leslie, R., Lin, P., Laskin, A., Laskin, J., and Nizkorodov, S. A.: Photochemistry of products of the aqueous reaction of methylglyoxal with ammonium sulfate, *ACS Earth Space Chem.*, 1, 522-532, <https://doi.org/10.1021/acsearthspacechem.7b00075>, 2017.

Al-Abadleh, H. A., Motaghedi, F., Mohammed, W., Rana, M. S., Malek, K. A., Rastogi, D., Asa-Awuku, A. A., and Guzman, M. I.: Reactivity of aminophenols in forming nitrogen-containing brown carbon from iron-catalyzed reactions, *Commun. Chem.*, 5, 112, <https://doi.org/10.1038/s42004-022-00732-1>, 2022.

972 Andreae, M. O. and Gelencsér, A.: Black carbon or brown carbon? The nature of
 973 light-absorbing carbonaceous aerosols, *Atmos. Chem. Phys.*, 6, 3131-3148,
 974 <https://doi.org/10.5194/acp-6-3131-2006>, 2006.

975 Aurell, J., Gullett, B. K., and Tabor, D.: Emissions from southeastern U.S.
 976 Grasslands and pine savannas: Comparison of aerial and ground field measurements
 977 with laboratory burns, *Atmos. Environ.*, 111, 170-178,
 978 <https://doi.org/10.1016/j.atmosenv.2015.03.001>, 2015.

979 Bae, E., Yeo, I. J., Jeong, B., Shin, Y., Shin, K. H., and Kim, S.: Study of double
 980 bond equivalents and the numbers of carbon and oxygen atom distribution of dissolved
 981 organic matter with negative-mode FT-ICR MS, *Analytical Chemistry*, 83, 4193-4199,
 982 <https://doi.org/10.1021/ac200464q>, 2011.

983 Bai, D. P., Wang, H. L., Tan, Y., Yin, Y., Wu, Z. J., Guo, S., Shen, L. J., Zhu, B.,
 984 Wang, J. H., and Kong, X. C.: Optical properties of aerosols and chemical composition
 985 apportionment under different pollution levels in Wuhan during January 2018,
 986 <https://doi.org/10.3390/atmos11010017>, 2020.

987 Barsotti, F., Ghigo, G., and Vione, D.: Computational assessment of the
 988 fluorescence emission of phenol oligomers: A possible insight into the fluorescence
 989 properties of humic-like substances (HULIS), *J. Photochem. Photobiol., A*, 315, 87-93,
 990 <https://doi.org/10.1016/j.jphotochem.2015.09.012>, 2016.

991 Bhowmik, H. S., Tripathi, S. N., Shukla, A. K., Lalchandani, V., Murari, V.,
 992 Devaprasad, M., Shivam, A., Bhushan, R., Pr é vôt, A. S. H., and Rastogi, N.:
 993 Contribution of fossil and biomass-derived secondary organic carbon to winter water-
 994 soluble organic aerosols in Delhi, India, *Sci. Total Environ.*, 912, 168655,
 995 <https://doi.org/10.1016/j.scitotenv.2023.168655>, 2024.

996 Birdwell, J. E. and Engel, A. S.: Characterization of dissolved organic matter in
 997 cave and spring waters using UV–Vis absorbance and fluorescence spectroscopy, *Org.*
 998 *Geochem.*, 41, 270-280, <https://doi.org/10.1016/j.orggeochem.2009.11.002>, 2010.

999 Bond, T. C. and Bergstrom, R. W.: Light absorption by carbonaceous particles: an

investigative review, *Aerosol Sci. Technol.*, 40, 27-67,
<https://doi.org/10.1080/02786820500421521>, 2006.

Bones, D. L., Henricksen, D. K., Mang, S. A., Gonsior, M., Bateman, A. P.,
 Nguyen, T. B., Cooper, W. J., and Nizkorodov, S. A.: Appearance of strong absorbers
 and fluorophores in limonene-O₃ secondary organic aerosol due to NH₄⁺-mediated
 chemical aging over long time scales, *J. Geophys. Res.: Atmos.*, 115,
<https://doi.org/10.1029/2009JD012864>, 2010.

Bozzetti, C., El Haddad, I., Salameh, D., Daellenbach, K. R., Fermo, P., Gonzalez,
 R., Minguillón, M. C., Iinuma, Y., Poulain, L., Elser, M., Müller, E., Slowik, J. G.,
 Jaffrezo, J. L., Baltensperger, U., Marchand, N., and Prévôt, A. S. H.: Organic aerosol
 source apportionment by offline-AMS over a full year in Marseille, *Atmos. Chem.*
Phys., 17, 8247-8268, <https://doi.org/10.5194/acp-17-8247-2017>, 2017.

Brown, H., Wang, H. L., Flanner, M., Liu, X. H., Singh, B., Zhang, R. D., Yang,
 Y., and Wu, M. X.: Brown Carbon Fuel and Emission Source Attributions to Global
 Snow Darkening Effect, *J ADV MODEL EARTH SY*, 14,
<https://doi.org/10.1029/2021ms002768>, 2022.

Budisulistiorini, S. H., Riva, M., Williams, M., Chen, J., Itoh, M., Surratt, J. D.,
 and Kuwata, M.: Light-absorbing brown carbon aerosol constituents from combustion
 of indonesian peat and biomass, *Environ. Sci. Technol.*, 51, 4415-4423,
<https://doi.org/10.1021/acs.est.7b00397>, 2017.

Cain, J., Laskin, A., Kholghy, M. R., Thomson, M. J., and Wang, H.: Molecular
 characterization of organic content of soot along the centerline of a coflow diffusion
 flame, *Phys. Chem. Chem. Phys.*, 16, 25862-25875,
<https://doi.org/10.1039/C4CP03330B>, 2014.

Canagaratna, M. R., Jayne, J. T., Ghertner, D. A., Herndon, S., Shi, Q., Jimenez, J.
 L., Silva, P. J., Williams, P., Lanni, T., Drewnick, F., Demerjian, K. L., Kolb, C. E., and
 Worsnop, D. R.: Chase studies of particulate emissions from in-use New York City
 vehicles, *Aerosol Sci. Technol.*, 38, 555-573,
<https://doi.org/10.1080/02786820490465504>, 2004.

1029 Canagaratna, M. R., Jimenez, J. L., Kroll, J. H., Chen, Q., Kessler, S. H., Massoli,
 1030 P., Hildebrandt Ruiz, L., Fortner, E., Williams, L. R., Wilson, K. R., Surratt, J. D.,
 1031 Donahue, N. M., Jayne, J. T., and Worsnop, D. R.: Elemental ratio measurements of
 1032 organic compounds using aerosol mass spectrometry: characterization, improved
 1033 calibration, and implications, *Atmos. Chem. Phys.*, 15, 253-272,
 1034 <https://doi.org/10.5194/acp-15-253-2015>, 2015.
 1035 Cao, T., Li, M. J., Zou, C. L., Fan, X. J., Song, J. Z., Jia, W. L., Yu, C. L., Yu, Z.
 1036 Q., and Peng, P. A.: Chemical composition, optical properties, and oxidative potential
 1037 of water- and methanol-soluble organic compounds emitted from the combustion of
 1038 biomass materials and coal, *Atmos. Chem. Phys.*, 21, 13187-13205,
 1039 <https://doi.org/10.5194/acp-21-13187-2021>, 2021.
 1040 Cavalli, F., Facchini, M. C., Decesari, S., Mircea, M., Emblico, L., Fuzzi, S.,
 1041 Ceburnis, D., Yoon, Y. J., O'Dowd, C. D., Putaud, J. P., and Dell'Acqua, A.: Advances
 1042 in characterization of size-resolved organic matter in marine aerosol over the North
 1043 Atlantic, *J. Geophys. Res.: Atmos.*, 109, <https://doi.org/10.1029/2004JD005137>, 2004.
 1044 Chakrabarty, R. K., Moosmüller, H., Chen, L. W. A., Lewis, K., Arnott, W. P.,
 1045 Mazzoleni, C., Dubey, M. K., Wold, C. E., Hao, W. M., and Kreidenweis, S. M.: Brown
 1046 carbon in tar balls from smoldering biomass combustion, *Atmos. Chem. Phys.*, 10,
 1047 6363-6370, <https://doi.org/10.5194/acp-10-6363-2010>, 2010.
 1048 Chakrabarty, R. K., Shetty, N. J., Thind, A. S., Beeler, P., Sumlin, B. J., Zhang, C.,
 1049 Liu, P., Idrobo, J. C., Adachi, K., Wagner, N. L., Schwarz, J. P., Ahern, A., Sedlacek, A.
 1050 J., 3rd, Lambe, A., Daube, C., Lyu, M., Liu, C., Herndon, S., Onasch, T. B., and Mishra,
 1051 R.: Shortwave absorption by wildfire smoke dominated by dark brown carbon, *Nat*
 1052 *Geosci.*, 16, 683-688, <https://doi.org/10.1038/s41561-023-01237-9>, 2023.
 1053 Chen, K. P., Raeofy, N., Lum, M., Mayorga, R., Woods, M., Bahreini, R., Zhang,
 1054 H. F., and Lin, Y. H.: Solvent effects on chemical composition and optical properties of
 1055 extracted secondary brown carbon constituents, *Aerosol Sci. Technol.*, 56, 917-930,
 1056 <https://doi.org/10.1080/02786826.2022.2100734>, 2022.
 1057 Chen, Q. C., Hua, X. Y., Li, J. W., Chang, T., and Wang, Y. Q.: Diurnal evolutions

1058 and sources of water-soluble chromophoric aerosols over Xi'an during haze event, in
 1059 Northwest China, *Sci. Total Environ.*, 786, 147412,
 1060 <https://doi.org/10.1016/j.scitotenv.2021.147412>, 2021.

1061 Chen, Q. C., Li, J. W., Hua, X. Y., Jiang, X. T., Mu, Z., Wang, M. M., Wang, J.,
 1062 Shan, M., Yang, X. D., Fan, X. J., Song, J. Z., Wang, Y. Q., Guan, D. J., and Du, L.:
 1063 Identification of species and sources of atmospheric chromophores by fluorescence
 1064 excitation-emission matrix with parallel factor analysis, *Sci. Total Environ.*, 718,
 1065 137322, <https://doi.org/10.1016/j.scitotenv.2020.137322>, 2020a.

1066 Chen, Q. C., Miyazaki, Y., Kawamura, K., Matsumoto, K., Coburn, S., Volkamer,
 1067 R., Iwamoto, Y., Kagami, S., Deng, Y. G., Ogawa, S. H., Ramasamy, S., Kato, S., Ida,
 1068 A., Kajii, Y., and Mochida, M.: Characterization of chromophoric water-soluble organic
 1069 matter in urban, forest, and marine aerosols by HR-ToF-AMS analysis and excitation–
 1070 emission matrix spectroscopy, *Environ. Sci. Technol.*, 50, 10351-10360,
 1071 <https://doi.org/10.1021/acs.est.6b01643>, 2016.

1072 Chen, Y. and Bond, T. C.: Light absorption by organic carbon from wood
 1073 combustion, *Atmos. Chem. Phys.*, 10, 1773-1787, [https://doi.org/10.5194/acp-10-](https://doi.org/10.5194/acp-10-1773-2010)
 1074 [1773-2010](https://doi.org/10.5194/acp-10-1773-2010), 2010.

1075 Chen, Y. F., Ge, X. L., Chen, H., Xie, X. C., Chen, Y. T., Wang, J. F., Ye, Z. L.,
 1076 Bao, M. Y., Zhang, Y. L., and Chen, M. D.: Seasonal light absorption properties of
 1077 water-soluble brown carbon in atmospheric fine particles in Nanjing, China, *Atmos.*
 1078 *Environ.*, 187, 230-240, <https://doi.org/10.1016/j.atmosenv.2018.06.002>, 2018.

1079 Chen, Y. F., Xie, X. C., Shi, Z., Li, Y. L., Gai, X. Y., Wang, J. F., Li, H. W., Wu, Y.,
 1080 Zhao, X. Y., Chen, M. D., and Ge, X. L.: Brown carbon in atmospheric fine particles in
 1081 Yangzhou, China: Light absorption properties and source apportionment, *Atmos. Res.*,
 1082 244, 105028, <https://doi.org/10.1016/j.atmosres.2020.105028>, 2020b.

1083 Cheng, Y., He, K. B., Du, Z. Y., Engling, G., Liu, J. M., Ma, Y. L., Zheng, M., and
 1084 Weber, R. J.: The characteristics of brown carbon aerosol during winter in Beijing,
 1085 *Atmos. Environ.*, 127, 355-364, <https://doi.org/10.1016/j.atmosenv.2015.12.035>, 2016.

1086 Coble, P. G.: Characterization of marine and terrestrial DOM in seawater using

1087 excitation-emission matrix spectroscopy, *Mar. Chem.*, 51, 325-346,
 1088 [https://doi.org/10.1016/0304-4203\(95\)00062-3](https://doi.org/10.1016/0304-4203(95)00062-3), 1996.

1089 Daellenbach, K. R., Stefenelli, G., Bozzetti, C., Vlachou, A., Fermo, P., Gonzalez,
 1090 R., Piazzalunga, A., Colombi, C., Canonaco, F., Hueglin, C., Kasper-Giebl, A., Jaffrezo,
 1091 J. L., Bianchi, F., Slowik, J. G., Baltensperger, U., El-Haddad, I., and Prévôt, A. S. H.:
 1092 Long-term chemical analysis and organic aerosol source apportionment at nine sites in
 1093 central Europe: source identification and uncertainty assessment, *Atmos. Chem. Phys.*,
 1094 17, 13265-13282, <https://doi.org/10.5194/acp-17-13265-2017>, 2017.

1095 DeLessio, M. A., Tsigaridis, K., Bauer, S. E., Chowdhary, J., and Schuster, G. L.:
 1096 Modeling atmospheric brown carbon in the GISS ModelE Earth system model, *Atmos.*
 1097 *Chem. Phys.*, 24, 6275-6304, <https://doi.org/10.5194/acp-24-6275-2024>, 2024.

1098 Deng, J. J., Ma, H., Wang, X. F., Zhong, S. J., Zhang, Z. M., Zhu, J. L., Fan, Y. B.,
 1099 Hu, W., Wu, L. B., Li, X. D., Ren, L. J., Pavuluri, C. M., Pan, X. L., Sun, Y. L., Wang,
 1100 Z. F., Kawamura, K., and Fu, P. Q.: Measurement report: Optical properties and sources
 1101 of water-soluble brown carbon in Tianjin, North China – insights from organic
 1102 molecular compositions, *Atmos. Chem. Phys.*, 22, 6449-6470,
 1103 <https://doi.org/10.5194/acp-22-6449-2022>, 2022.

1104 Dey, S., Mukherjee, A., Polana, A. J., Rana, A., Mao, J. Y., Jia, S. G., Yadav, A. K.,
 1105 Khillare, P. S., and Sarkar, S.: Brown carbon aerosols in the Indo-Gangetic Plain
 1106 outflow: insights from excitation emission matrix (EEM) fluorescence spectroscopy,
 1107 *Environ. Sci.: Processes Impacts*, 23, 745-755, <https://doi.org/10.1039/D1EM00050K>,
 1108 2021.

1109 Dong, W. M., Wan, J. M., Tokunaga, T. K., Gilbert, B., and Williams, K. H.:
 1110 Transport and humification of dissolved organic matter within a semi-arid floodplain,
 1111 *J. Environ. Sci.*, 57, 24-32, <https://doi.org/10.1016/j.jes.2016.12.011>, 2017.

1112 Dührkop, K., Fleischauer, M., Ludwig, M., Aksenov, A. r. A., Melnik, A. V.,
 1113 Meusel, M., Dorrestein, P. r. C., Rousu, J., and Böcker, S.: SIRIUS 4: a rapid tool for
 1114 turning tandem mass spectra into metabolite structure information, *Nat. Methods*, 16,

1115 299-302, <https://doi.org/10.1038/s41592-019-0344-8>, 2019.

1116 Fan, X. J., Wei, S. Y., Zhu, M. B., Song, J. Z., and Peng, P. A.: Comprehensive
 1117 characterization of humic-like substances in smoke PM_{2.5} emitted from the combustion
 1118 of biomass materials and fossil fuels, *Atmos. Chem. Phys.*, 16, 13321-13340,
 1119 <https://doi.org/10.5194/acp-16-13321-2016>, 2016.

1120 Fan, X. J., Yu, X. F., Wang, Y., Xiao, X., Li, F. Y., Xie, Y., Wei, S. Y., Song, J. Z.,
 1121 and Peng, P. A.: The aging behaviors of chromophoric biomass burning brown carbon
 1122 during dark aqueous hydroxyl radical oxidation processes in laboratory studies, *Atmos.*
 1123 *Environ.*, 205, 9-18, <https://doi.org/10.1016/j.atmosenv.2019.02.039>, 2019.

1124 Fan, Y., Liu, C. Q., Li, L., Ren, L., Ren, H., Zhang, Z., Li, Q., Wang, S., Hu, W.,
 1125 Deng, J., Wu, L., Zhong, S., Zhao, Y., Pavuluri, C. M., Li, X., Pan, X., Sun, Y., Wang,
 1126 Z., Kawamura, K., Shi, Z., and Fu, P.: Large contributions of biogenic and
 1127 anthropogenic sources to fine organic aerosols in Tianjin, North China, *Atmos. Chem.*
 1128 *Phys.*, 20, 117-137, <https://doi.org/10.5194/acp-20-117-2020>, 2020.

1129 Fasola, S., Maio, S., Baldacci, S., La Grutta, S., Ferrante, G., Forastiere, F.,
 1130 Stafoggia, M., Gariazzo, C., and Viegi, G.: Effects of particulate matter on the incidence
 1131 of respiratory diseases in the pisan longitudinal study, *Int. J. Environ. Res. Public Health*,
 1132 17, <https://doi.org/10.3390/ijerph17072540>, 2020.

1133 Feng, Y., Ramanathan, V., and Kotamarthi, V. R.: Brown carbon: a significant
 1134 atmospheric absorber of solar radiation?, *Atmos. Chem. Phys.*, 13, 8607-8621,
 1135 <https://doi.org/10.5194/acp-13-8607-2013>, 2013.

1136 Fleming, L. T., Lin, P., Roberts, J. M., Selimovic, V., Yokelson, R., Laskin, J.,
 1137 Laskin, A., and Nizkorodov, S. A.: Molecular composition and photochemical lifetimes
 1138 of brown carbon chromophores in biomass burning organic aerosol, *Atmos. Chem.*
 1139 *Phys.*, 20, 1105-1129, <https://doi.org/10.5194/acp-20-1105-2020>, 2020.

1140 Fu, P. Q., Kawamura, K., Chen, J., Qin, M. Y., Ren, L. J., Sun, Y. L., Wang, Z. F.,
 1141 Barrie, L. A., Tachibana, E., Ding, A. J., and Yamashita, Y.: Fluorescent water-soluble
 1142 organic aerosols in the High Arctic atmosphere, *Sci. Rep.*, 5, 9845,
 1143 <https://doi.org/10.1038/srep09845>, 2015.

1144 Ge, X. L., Wexler, A. S., and Clegg, S. L.: Atmospheric amines – part I. a review,
 1145 Atmos. Environ., 45, 524-546, <https://doi.org/10.1016/j.atmosenv.2010.10.012>, 2011.

1146 Ge, X. L., Sun, Y. L., Trousdell, J., Chen, M. D., and Zhang, Q.: Enhancing
 1147 characterization of organic nitrogen components in aerosols and droplets using high-
 1148 resolution aerosol mass spectrometry, Atmos. Meas. Tech., 17, 423-439,
 1149 <https://doi.org/10.5194/amt-17-423-2024>, 2024.

1150 Ge, X. L., Li, L., Chen, Y. F., Chen, H., Wu, D., Wang, J. F., Xie, X. C., Ge, S., Ye,
 1151 Z. L., Xu, J. Z., and Chen, M. D.: Aerosol characteristics and sources in Yangzhou,
 1152 China resolved by offline aerosol mass spectrometry and other techniques, Environ.
 1153 Pollut., 225, 74-85, <https://doi.org/10.1016/j.envpol.2017.03.044>, 2017.

1154 Gilardoni, S., Massoli, P., Paglione, M., Giulianelli, L., Carbone, C., Rinaldi, M.,
 1155 Decesari, S., Sandrini, S., Costabile, F., Gobbi, G. P., Pietrogrande, M. C., Visentin, M.,
 1156 Scotto, F., Fuzzi, S., and Facchini, M. C.: Direct observation of aqueous secondary
 1157 organic aerosol from biomass-burning emissions, Proc. Natl. Acad. Sci. U. S. A., 113,
 1158 10013-10018, <https://doi.org/10.1073/pnas.1602212113>, 2016.

1159 González, C., Mira-M., J., and Juárez, I.: Important variable assessment and
 1160 electricity price forecasting based on regression tree models: classification and
 1161 regression trees, Bagging and Random Forests, IET Gener. Transm. Dis., 9, 1120-1128,
 1162 <https://doi.org/10.1049/iet-gtd.2014.0655>, 2015.

1163 Gu, C. J., Cui, S. J., Ge, X. L., Wang, Z. Y., Chen, M. J., Qian, Z. H., Liu, Z. Y.,
 1164 Wang, X. F., and Zhang, Y. J.: Chemical composition, sources and optical properties of
 1165 nitrated aromatic compounds in fine particulate matter during winter foggy days in
 1166 Nanjing, China, Environ. Res., 212, 113255,
 1167 <https://doi.org/10.1016/j.envres.2022.113255>, 2022.

1168 Hawkins, L. N., Lemire, A. N., Galloway, M. M., Corrigan, A. L., Turley, J. J.,
 1169 Espelien, B. M., and De H., D. O.: Maillard chemistry in clouds and aqueous aerosol
 1170 as a source of atmospheric humic-like substances, Environ. Sci. Technol., 50, 7443-
 1171 7452, <https://doi.org/10.1021/acs.est.6b00909>, 2016.

1172 Hecobian, A., Zhang, X., Zheng, M., Frank, N., Edgerton, E. S., and Weber, R. J.:

1173 Water-soluble organic aerosol material and the light-absorption characteristics of
 1174 aqueous extracts measured over the southeastern United States, *Atmos. Chem. Phys.*, 10,
 1175 5965-5977, <https://doi.org/10.5194/acp-10-5965-2010>, 2010.
 1176 Hu, J. L., Wang, P., Ying, Q., Zhang, H. L., Chen, J. J., Ge, X. L., Li, X. H., Jiang,
 1177 J. K., Wang, S. X., Zhang, J., Zhao, Y., and Zhang, Y. Y.: Modeling biogenic and
 1178 anthropogenic secondary organic aerosol in China, *Atmos. Chem. Phys.*, 17, 77-92,
 1179 <https://doi.org/10.5194/acp-17-77-2017>, 2017.
 1180 Hu, R. L., Xu, Q. C., Wang, S. X., Hua, Y., Bhattarai, N., Jiang, J. K., Song, Y.,
 1181 Daellenbach, K. R., Qi, L., Prevot, A. S. H., and Hao, J. M.: Chemical characteristics
 1182 and sources of water-soluble organic aerosol in southwest suburb of Beijing, *J. Environ.*
 1183 *Sci.*, 95, 99-110, <https://doi.org/10.1016/j.jes.2020.04.004>, 2020.
 1184 Huang, L. B., Liu, T. S., and Grassian, V. i. H.: Radical-initiated formation of
 1185 aromatic organosulfates and sulfonates in the aqueous phase, *Environ. Sci. Technol.*,
 1186 54, 11857-11864, <https://doi.org/10.1021/acs.est.0c05644>, 2020.
 1187 Huang, R. J., Yang, L., Shen, J. C., Yuan, W., Gong, Y. Q., Ni, H. Y., Duan, J., Yan,
 1188 J., Huang, H. B., You, Q. H., and Li, Y. J.: Chromophoric fingerprinting of brown
 1189 carbon from residential biomass burning, *Environ. Sci. Technol. Lett.*, 9, 102-111,
 1190 <https://doi.org/10.1021/acs.estlett.1c00837>, 2022.
 1191 Huang, R. J., Yang, L., Cao, J. J., Chen, Y., Chen, Q., Li, Y. J., Duan, J., Zhu, C.
 1192 S., Dai, W. T., Wang, K., Lin, C. S., Ni, H. Y., Corbin, J. C., Wu, Y. F., Zhang, R. J., Tie,
 1193 X. X., Hoffmann, T., O'Dowd, C., and Dusek, U.: Brown carbon aerosol in urban Xi'
 1194 an, northwest China: the composition and light absorption properties, *Environ. Sci.*
 1195 *Technol.*, 52, 6825-6833, <https://doi.org/10.1021/acs.est.8b02386>, 2018.
 1196 Huguet, A., Vacher, L., Relexans, S., Saubusse, S., Froidefond, J. M., and Parlanti,
 1197 E.: Properties of fluorescent dissolved organic matter in the Gironde Estuary, *Org.*
 1198 *Geochem.*, 40, 706-719, <https://doi.org/10.1016/j.orggeochem.2009.03.002>, 2009.
 1199 Jacobson, M. Z.: Isolating nitrated and aromatic aerosols and nitrated aromatic
 1200 gases as sources of ultraviolet light absorption, *J. Geophys. Res.: Atmos.*, 104, 3527-
 1201 3542, <https://doi.org/10.1029/1998JD100054>, 1999.

1202 Jaoui, M., Corse, E., Kleindienst, T. E., Offenberg, J. H., Lewandowski, M., and
 1203 Edney, E. O.: Analysis of secondary organic aerosol compounds from the
 1204 photooxidation of d-limonene in the presence of NOX and their detection in ambient
 1205 PM2.5, *Environ. Sci. Technol.*, 40, 3819-3828, <https://doi.org/10.1021/es052566z>,
 1206 2006.

1207 Jiang, W. Q., Misovich, M. V., Hettiyadura, A. P. S., Laskin, A., McFall, A. S.,
 1208 Anastasio, C., and Zhang, Q.: Photosensitized Reactions of a phenolic carbonyl from
 1209 wood combustion in the aqueous phase—chemical evolution and light absorption
 1210 properties of aqSOA, *Environ. Sci. Technol.*, 55, 5199-5211,
 1211 <https://doi.org/10.1021/acs.est.0c07581>, 2021.

1212 Jiang, X. T., Liu, D. T., Li, Q., Tian, P., Wu, Y. Z., Li, S. Y., Hu, K., Ding, S., Bi,
 1213 K., Li, R. J., Huang, M. Y., Ding, D. P., Chen, Q. C., Kong, S. F., Li, W. J., Pang, Y.,
 1214 and He, D.: Connecting the light absorption of atmospheric organic aerosols with
 1215 oxidation state and polarity, *Environ. Sci. Technol.*, 56, 12873-12885,
 1216 <https://doi.org/10.1021/acs.est.2c02202>, 2022.

1217 Jo, D. S., Park, R. J., Lee, S., Kim, S. W., and Zhang, X.: A global simulation of
 1218 brown carbon: implications for photochemistry and direct radiative effect, *Atmos.*
 1219 *Chem. Phys.*, 16, 3413-3432, <https://doi.org/10.5194/acp-16-3413-2016>, 2016.

1220 Kim, H. J., Collier, S., Ge, X. L., Xu, J. Z., Sun, Y. L., Jiang, W. Q., Wang, Y. L.,
 1221 Herckes, P., and Zhang, Q.: Chemical processing of water-soluble species and
 1222 formation of secondary organic aerosol in fogs, *Atmos. Environ.*, 200, 158-166,
 1223 <https://doi.org/10.1016/j.atmosenv.2018.11.062>, 2019.

1224 Kourtchev, I., O'Connor, I. P., Giorio, C., Fuller, S. J., Kristensen, K., Maenhaut,
 1225 W., Wenger, J. C., Sodeau, J. R., Glasius, M., and Kalberer, M.: Effects of
 1226 anthropogenic emissions on the molecular composition of urban organic aerosols: An
 1227 ultrahigh resolution mass spectrometry study, *Atmos. Environ.*, 89, 525-532,
 1228 <https://doi.org/10.1016/j.atmosenv.2014.02.051>, 2014.

1229 Kroll, J. H., Donahue, N. M., Jimenez, J. L., Kessler, S. H., Canagaratna, M. R.,
 1230 Wilson, K. R., Altieri, K. E., Mazzoleni, L. R., Wozniak, A. S., Bluhm, H., Mysak, E.

1231 R., Smith, J. D., Kolb, C. E., and Worsnop, D. R.: Carbon oxidation state as a metric
 1232 for describing the chemistry of atmospheric organic aerosol, *Nat. Chem.*, 3, 133-139,
 1233 <https://doi.org/10.1038/nchem.948>, 2011.

1234 Kuang, Y., Shang, J., and Chen, Q. C.: Effect of ozone aging on light absorption
 1235 and fluorescence of brown carbon in soot particles: The important role of polycyclic
 1236 aromatic hydrocarbons, *J. Hazard. Mater.*, 413, 125406,
 1237 <https://doi.org/10.1016/j.jhazmat.2021.125406>, 2021.

1238 Kuang, Y., Shang, J., Sheng, M. S., Shi, X. D., Zhu, J. L., and Qiu, X. H.:
 1239 Molecular Composition of Beijing PM(2.5) Brown Carbon Revealed by an Untargeted
 1240 Approach Based on Gas Chromatography and Time-of-Flight Mass Spectrometry,
 1241 *Environ. Sci. Technol.*, 57, 909-919, <https://doi.org/10.1021/acs.est.2c05918>, 2023.

1242 Kumar, V., Giannoukos, S., Haslett, S. L., Tong, Y., Singh, A., Bertrand, A., Lee,
 1243 C. P., Wang, D. S., Bhattu, D., Stefenelli, G., Dave, J. S., Puthussery, J. V., Qi, L., Vats,
 1244 P., Rai, P., Casotto, R., Satish, R., Mishra, S., Pospisilova, V., Mohr, C., Bell, D. M.,
 1245 Ganguly, D., Verma, V., Rastogi, N., Baltensperger, U., Tripathi, S. N., Prévôt, A. S. H.,
 1246 and Slowik, J. G.: Highly time-resolved chemical speciation and source apportionment
 1247 of organic aerosol components in Delhi, India, using extractive electrospray ionization
 1248 mass spectrometry, *Atmos. Chem. Phys.*, 22, 7739-7761, [https://10.5194/acp-22-7739-](https://10.5194/acp-22-7739-2022)
 1249 [2022](https://10.5194/acp-22-7739-2022), 2022.

1250 Laskin, A., Laskin, J., and Nizkorodov, S. A.: Chemistry of atmospheric brown
 1251 carbon, *Chem. Rev.*, 115, 4335-4382, <https://doi.org/10.1021/cr5006167>, 2015.

1252 Laskin, A., Smith, J. S., and Laskin, J.: Molecular characterization of nitrogen-
 1253 containing organic compounds in biomass burning aerosols using high-resolution mass
 1254 spectrometry, *Environ. Sci. Technol.*, 43, 3764-3771,
 1255 <https://doi.org/10.1021/es803456n>, 2009.

1256 Laskin, A., West, C. P., and Hettiyadura, A. P. S.: Molecular insights into the
 1257 composition, sources, and aging of atmospheric brown carbon, *Chem Soc Rev*, 54,
 1258 1583-1612, [10.1039/d3cs00609c](https://doi.org/10.1039/d3cs00609c), 2025.

1259 Lee, H. L., Laskin, A., Laskin, J., and Nizkorodov, S. A.: Excitation–emission

1260 spectra and fluorescence quantum yields for fresh and aged biogenic secondary organic
 1261 aerosols, *Environ. Sci. Technol.*, 47, 5763-5770, <https://doi.org/10.1021/es400644c>,
 1262 2013.

1263 Lei, R. Y., Sha, Y. Y., Meng, H. F., Huang, Y., Ye, J. H., Huang, D. D., Zhang, Y.
 1264 J., Wu, Y., Li, Y. J., and Ge, X. L.: Aqueous phase photolysis of 4-nitrocatechol:
 1265 Reaction kinetics, evolutions of chemical composition, light absorption and oxidation
 1266 potential, *Atmos. Environ.*, 343, 120981,
 1267 <https://doi.org/10.1016/j.atmosenv.2024.120981>, 2025.

1268 Li, H., Qin, X. F., Wang, G. C., Xu, J., Wang, Lu, D., Liu, C., Zheng, H., Liu, J.
 1269 G., Huang, K., and Deng, C. R.: Conjoint impacts of continental outflows and marine
 1270 sources on brown carbon in the East China sea: Abundances, optical properties, and
 1271 formation processes, *Atmos. Environ.*, 273, 118959,
 1272 <https://doi.org/10.1016/j.atmosenv.2022.118959>, 2022a.

1273 Li, H. W., Cui, L., Huang, Y., Zhang, Y. J., Wang, J. F., Chen, M. D., and Ge, X.
 1274 L.: Concurrent dominant pathways of multifunctional products formed from nocturnal
 1275 isoprene oxidation, *Chemosphere*, 322, 138185,
 1276 <https://doi.org/10.1016/j.chemosphere.2023.138185>, 2023.

1277 Li, M., Wang, X. F., Lu, C. Y., Li, R., Zhang, J., Dong, S. W., Yang, L. X., Xue, L.,
 1278 Chen, J. M., and Wang, W. X.: Nitrated phenols and the phenolic precursors in the
 1279 atmosphere in urban Jinan, China, *Sci. Total Environ.*, 714, 136760,
 1280 <https://doi.org/10.1016/j.scitotenv.2020.136760>, 2020.

1281 Li, M. J., Fan, X. J., Zhu, M. B., Zou, C. L., Song, J. Z., Wei, S. Y., Jia, W. L., and
 1282 Peng, P. A.: Abundance and light absorption properties of brown carbon emitted from
 1283 residential coal combustion in China, *Environ. Sci. Technol.*, 53, 595-603,
 1284 <https://doi.org/10.1021/acs.est.8b05630>, 2019.

1285 Li, S., Chen, C., Yang, G.-l., Fang, J., Sun, Y., Tang, L., Wang, H., Xiang, W.,
 1286 Zhang, H., Croteau, P. L., Jayne, J. T., Liao, H., Ge, X., Favez, O., and Zhang, Y.:
 1287 Sources and processes of organic aerosol in non-refractory PM1 and PM2.5 during
 1288 foggy and haze episodes in an urban environment of the Yangtze River Delta, China,

1289 Environ. Res., 212, 113557, <https://doi.org/10.1016/j.envres.2022.113557>, 2022b.
 1290 Li, X. D., Tao, Y., Zhu, L. W., Ma, S. S., Luo, S. P., Zhao, Z. Z., Sun, N., Ge, X.
 1291 L., and Ye, Z. L.: Optical and chemical properties and oxidative potential of aqueous-
 1292 phase products from OH and 3C*-initiated photooxidation of eugenol, Atmos. Chem.
 1293 Phys., 22, 7793-7814, <https://doi.org/10.5194/acp-22-7793-2022>, 2022c.
 1294 Lin, G. X., Penner, J. E., Flanner, M. G., Sillman, S., Xu, L., and Zhou, C.:
 1295 Radiative forcing of organic aerosol in the atmosphere and on snow: effects of SOA
 1296 and brown carbon, J. Geophys. Res.: Atmos., 119, 7453-7476,
 1297 <https://doi.org/10.1002/2013JD021186>, 2014.
 1298 Lin, P., Rincon, A. G., Kalberer, M., and Yu, J. Z.: Elemental composition of
 1299 HULIS in the pearl river delta region, China: results inferred from positive and negative
 1300 electrospray high resolution mass spectrometric data, Environ. Sci. Technol., 46, 7454-
 1301 7462, <https://doi.org/10.1021/es300285d>, 2012.
 1302 Lin, P., Fleming, L. T., Nizkorodov, S. A., Laskin, J., and Laskin, A.:
 1303 Comprehensive molecular characterization of atmospheric brown carbon by high
 1304 resolution mass spectrometry with electrospray and atmospheric pressure
 1305 photoionization, Anal. Chem., 90, 12493-12502,
 1306 <https://doi.org/10.1021/acs.analchem.8b02177>, 2018.
 1307 Lin, P., Bluvshstein, N., Rudich, Y., Nizkorodov, S. A., Laskin, J., and Laskin, A.:
 1308 Molecular chemistry of atmospheric brown carbon inferred from a nationwide biomass
 1309 burning event, Environ. Sci. Technol., 51, 11561-11570,
 1310 <https://doi.org/10.1021/acs.est.7b02276>, 2017.
 1311 Lin, P., Liu, J. M., Shilling, J. E., Kathmann, S. M., Laskin, J., and Laskin, A.:
 1312 Molecular characterization of brown carbon (BrC) chromophores in secondary organic
 1313 aerosol generated from photo-oxidation of toluene, Phys. Chem. Chem. Phys., 17,
 1314 23312-23325, <https://doi.org/10.1039/C5CP02563J>, 2015.
 1315 Lin, P., Aiona, P. K., Li, Y., Shiraiwa, M., Laskin, J., Nizkorodov, S. A., and Laskin,
 1316 A.: Molecular characterization of brown carbon in biomass burning aerosol particles,
 1317 Environ. Sci. Technol., 50, 11815-11824, <https://doi.org/10.1021/acs.est.6b03024>,

2016.

Liu, Y., Li, H. W., Cui, S. J., Nie, D. Y., Chen, Y. F., and Ge, X. L.: Chemical Characteristics and Sources of Water-Soluble Organic Nitrogen Species in PM_{2.5} in Nanjing, China, <https://doi.org/10.3390/atmos12050574>, 2021.

Lobodin, V. V., Marshall, A. G., and Hsu, C. S.: Compositional space boundaries for organic compounds, *Analytical Chemistry*, 84, 3410-3416, <https://doi.org/10.1021/ac300244f>, 2012.

Ma, Y. L. and Hays, M. D.: Thermal extraction – two-dimensional gas chromatography–mass spectrometry with heart-cutting for nitrogen heterocyclics in biomass burning aerosols, *J. Chromatogr. A*, 1200, 228-234, <https://doi.org/10.1016/j.chroma.2008.05.078>, 2008.

Mao, J. F., Cheng, Y., Bai, Z., Zhang, W., Zhang, L. Y., Chen, H., Wang, L. N., Li, L., and Chen, J. M.: Molecular characterization of nitrogen-containing organic compounds in the winter North China Plain, *Sci Total Environ*, 838, 156189, <https://doi.org/10.1016/j.scitotenv.2022.156189>, 2022.

Matos, J. T. V., Freire, S. M. S. C., Duarte, R. M. B. O., and Duarte, A. C.: Natural organic matter in urban aerosols: comparison between water and alkaline soluble components using excitation–emission matrix fluorescence spectroscopy and multiway data analysis, *Atmos. Environ.*, 102, 1-10, <https://doi.org/10.1016/j.atmosenv.2014.11.042>, 2015.

McKnight, D. M., Boyer, E. W., Westerhoff, P. K., Doran, P. T., Kulbe, T., and Andersen, D. T.: Spectrofluorometric characterization of dissolved organic matter for indication of precursor organic material and aromaticity, *Limnol. Oceanogr.*, 46, 38-48, <https://doi.org/10.4319/lo.2001.46.1.0038>, 2001.

McNeill, V. F.: Aqueous organic chemistry in the atmosphere: sources and chemical processing of organic aerosols, *Environ. Sci. Technol.*, 49, 1237-1244, <https://doi.org/10.1021/es5043707>, 2015.

Murphy, K. R., Stedmon, C. A., Graeber, D., and Bro, R.: Fluorescence

1346 spectroscopy and multi-way techniques. PARAFAC, *Anal. Methods*, 5,
 1347 <https://doi.org/10.1039/c3ay41160e>, 2013.

1348 Murphy, K. R., Hambly, A., Singh, S., Henderson, R. K., Baker, A., Stuetz, R., and
 1349 Khan, S. J.: Organic matter fluorescence in municipal water recycling schemes: toward
 1350 a unified PARAFAC model, *Environ. Sci. Technol.*, 45, 2909-2916,
 1351 <https://doi.org/10.1021/es103015e>, 2011.

1352 Negron-Encarnacion, I. and Arce, R.: Light-induced transformations of aza-
 1353 aromatic pollutants adsorbed on models of atmospheric particulate matter: Acridine and
 1354 9(10-H) acridone, *Atmos. Environ.*, 41, 6771-6783,
 1355 <https://doi.org/10.1016/j.atmosenv.2007.04.062>, 2007.

1356 O'Brien, R. E., Ridley, K. J., Canagaratna, M. R., Jayne, J. T., Croteau, P. L.,
 1357 Worsnop, D. R., Budisulistiorini, S. H., Surratt, J. D., Follett, C. L., Repeta, D. J., and
 1358 Kroll, J. H.: Ultrasonic nebulization for the elemental analysis of microgram-level
 1359 samples with offline aerosol mass spectrometry, *Atmos. Meas. Tech.*, 12, 1659-1671,
 1360 <https://doi.org/10.5194/amt-12-1659-2019>, 2019.

1361 Onasch, T. B., Trimborn, A., Fortner, E. C., Jayne, J. T., Kok, G. L., Williams, L.
 1362 R., Davidovits, P., and Worsnop, D. R.: Soot particle aerosol mass spectrometer:
 1363 development, validation, and initial application, *Aerosol Sci. Technol.*, 46, 804-817,
 1364 <https://doi.org/10.1080/02786826.2012.663948>, 2012.

1365 Ou, Y., Nie, D. Y., Chen, H., Ye, Z. L., and Ge, X. L.: Characterization of products
 1366 from the aqueous-phase photochemical oxidation of benzene-diols, *Atmosphere*, 12,
 1367 <https://doi.org/10.3390/atmos12050534>, 2021.

1368 Petters, S. S., Cui, T. Q., Zhang, Z. F., Gold, A., McNeill, V. F., Surratt, J. D., and
 1369 Turpin, B. J.: Organosulfates from dark aqueous reactions of isoprene-derived
 1370 epoxydiols under cloud and fog conditions: kinetics, mechanism, and effect of reaction
 1371 environment on regioselectivity of sulfate addition, *ACS Earth Space Chem.*, 5, 474-
 1372 486, <https://doi.org/10.1021/acsearthspacechem.0c00293>, 2021.

1373 Powelson, M. H., Espelien, B. M., Hawkins, L. N., Galloway, M. M., and De Haan,
 1374 D. O.: Brown Carbon Formation by Aqueous-Phase Carbonyl Compound Reactions

1375 with Amines and Ammonium Sulfate, *Environ. Sci. Technol.*, 48, 985-993,
 1376 <https://doi.org/10.1021/es4038325>, 2014.

1377 Qi, L., Chen, M. D., Stefenelli, G., Pospisilova, V., Tong, Y. D., Bertrand, A.,
 1378 Hueglin, C., Ge, X. L., Baltensperger, U., Prévôt, A. S. H., and Slowik, J. G.: Organic
 1379 aerosol source apportionment in Zurich using an extractive electrospray ionization
 1380 time-of-flight mass spectrometer (EESI-TOF-MS) – Part 2: biomass burning
 1381 influences in winter, *Atmos. Chem. Phys.*, 19, 8037-8062, [https://doi.org/10.5194/acp-](https://doi.org/10.5194/acp-19-8037-2019)
 1382 [19-8037-2019](https://doi.org/10.5194/acp-19-8037-2019), 2019.

1383 Qin, J. J., Zhang, L. M., Zhou, X. M., Duan, J. C., Mu, S. T., Xiao, K., Hu, J. N.,
 1384 and Tan, J. H.: Fluorescence fingerprinting properties for exploring water-soluble
 1385 organic compounds in PM_{2.5} in an industrial city of northwest China, *Atmos. Environ.*,
 1386 184, 203-211, <https://doi.org/10.1016/j.atmosenv.2018.04.049>, 2018.

1387 Qin, Y. M., Tan, H. B., Li, Y. J., Schurman, M. I., Li, F., Canonaco, F., Prévôt, A.
 1388 S. H., and Chan, C. K.: Impacts of traffic emissions on atmospheric particulate nitrate
 1389 and organics at a downwind site on the periphery of Guangzhou, China, *Atmos. Chem.*
 1390 *Phys.*, 17, 10245-10258, <https://doi.org/10.5194/acp-17-10245-2017>, 2017.

1391 Qiu, Y. M., Xie, Q. R., Wang, J. F., Xu, W. Q., Li, L. J., Wang, Q. Q., Zhao, J.,
 1392 Chen, Y. T., Chen, Y. F., Wu, Y. Z., Du, W., Zhou, W., Lee, J., Zhao, C. F., Ge, X. L.,
 1393 Fu, P. Q., Wang, Z., Worsnop, D. R., and Sun, Y. L.: Vertical characterization and source
 1394 apportionment of water-soluble organic aerosol with high-resolution aerosol mass
 1395 spectrometry in Beijing, China, *ACS Earth Space Chem.*, 3, 273-284,
 1396 <https://doi.org/10.1021/acsearthspacechem.8b00155>, 2019.

1397 Shapiro, E. L., Szprengiel, J., Sareen, N., Jen, C. N., Giordano, M. R., and McNeill,
 1398 V. F.: Light-absorbing secondary organic material formed by glyoxal in aqueous aerosol
 1399 mimics, *Atmos. Chem. Phys.*, 9, 2289-2300, <https://doi.org/10.5194/acp-9-2289-2009>,
 1400 2009.

1401 Song, J. Z., Li, M. J., Fan, X. J., Zou, C. L., Zhu, M. B., Jiang, B., Yu, Z. Q., Jia,
 1402 W. L., Liao, Y. H., and Peng, P. A.: Molecular Characterization of water- and methanol-

soluble organic compounds emitted from residential coal combustion using ultrahigh-resolution electrospray ionization fourier transform ion cyclotron resonance mass spectrometry, *Environ. Sci. Technol.*, 53, 13607-13617, <https://doi.org/10.1021/acs.est.9b04331>, 2019.

Stubbins, A., Lapierre, J. F., Berggren, M., Prairie, Y. T., Dittmar, T., and del Giorgio, P. A.: What's in an EEM? Molecular Signatures Associated with Dissolved Organic Fluorescence in Boreal Canada, *Environ. Sci. Technol.*, 48, 10598-10606, <https://doi.org/10.1021/es502086e>, 2014.

Sun, Y. L., Du, W., Fu, P. Q., Wang, Q. Q., Li, J., Ge, X. L., Zhang, Q., Zhu, C. M., Ren, L. J., Xu, W. Q., Zhao, J., Han, T. T., Worsnop, D. R., and Wang, Z.: Primary and secondary aerosols in Beijing in winter: sources, variations and processes, *Atmos. Chem. Phys.*, 16, 8309-8329, <https://doi.org/10.5194/acp-16-8309-2016>, 2016.

Tang, J., Li, J., Su, T., Han, Y., Mo, Y. Z., Jiang, H. X., Cui, M., Jiang, B., Chen, Y. J., Tang, J. H., Song, J. Z., Peng, P. A., and Zhang, G.: Molecular compositions and optical properties of dissolved brown carbon in biomass burning, coal combustion, and vehicle emission aerosols illuminated by excitation–emission matrix spectroscopy and Fourier transform ion cyclotron resonance mass spectrometry analysis, *Atmos. Chem. Phys.*, 20, 2513-2532, <https://doi.org/10.5194/acp-20-2513-2020>, 2020.

Tang, J., Li, J., Zhao, S. Z., Zhong, G. C., Mo, Y. Z., Jiang, H. X., Jiang, B., Chen, Y. J., Tang, J. H., Tian, C. G., Zong, Z., Hussain S., J., Song, J. Z., and Zhang, G.: Molecular signatures and formation mechanisms of water-soluble chromophores in particulate matter from Karachi in Pakistan, *Sci. Total Environ.*, 914, 169890, <https://doi.org/10.1016/j.scitotenv.2024.169890>, 2024.

Tsugawa, H., Cajka, T., Kind, T., Ma, Y., Higgins, B., Ikeda, K., Kanazawa, M., VanderGheynst, J., Fiehn, O., and Arita, M.: MS-DIAL: data-independent MS/MS deconvolution for comprehensive metabolome analysis, *Nat. Methods*, 12, 523-526, <https://doi.org/10.1038/nmeth.3393>, 2015.

Ulbrich, I. M., Canagaratna, M. R., Zhang, Q., Worsnop, D. R., and Jimenez, J. L.: Interpretation of organic components from Positive Matrix Factorization of aerosol

1432 mass spectrometric data, *Atmos. Chem. Phys.*, 9, 2891-2918,
 1433 <https://doi.org/10.5194/acp-9-2891-2009>, 2009.

1434 Updyke, K. M., Nguyen, T. B., and Nizkorodov, S. A.: Formation of brown carbon
 1435 via reactions of ammonia with secondary organic aerosols from biogenic and
 1436 anthropogenic precursors, *Atmos. Environ.*, 63, 22-31,
 1437 <https://doi.org/10.1016/j.atmosenv.2012.09.012>, 2012.

1438 Vasilakopoulou, C. N., Florou, K., Kaltsonoudis, C., Stavroulas, I., Mihalopoulos,
 1439 N., and Pandis, S. N.: Development and evaluation of an improved offline aerosol mass
 1440 spectrometry technique, *Atmos. Meas. Tech.*, 16, 2837-2850,
 1441 <https://doi.org/10.5194/amt-16-2837-2023>, 2023.

1442 Veld, M., Khare, P., Hao, Y. F., Reche, C., Pérez, N., Alastuey, A., Yus-Díez, J.,
 1443 Marchand, N., Prevot, A. S. H., Querol, X., and Daellenbach, K. R.: Characterizing the
 1444 sources of ambient PM₁₀ organic aerosol in urban and rural Catalonia, Spain, *Sci. Total*
 1445 *Environ.*, 902, 166440, <https://doi.org/10.1016/j.scitotenv.2023.166440>, 2023.

1446 Wang, D. W., Shen, Z. X., Zhang, Q., Lei, Y. L., Zhang, T., Huang, S. S., Sun, J.,
 1447 Xu, H. M., and Cao, J. J.: Winter brown carbon over six of China's megacities: light
 1448 absorption, molecular characterization, and improved source apportionment revealed
 1449 by multilayer perceptron neural network, *Atmos. Chem. Phys.*, 22, 14893-14904,
 1450 <https://doi.org/10.5194/acp-22-14893-2022>, 2022a.

1451 Wang, J. F., Ge, X. L., Sonya, C., Ye, J. H., Lei, Y. L., Chen, M. D., and Zhang, Q.:
 1452 Influence of regional emission controls on the chemical composition, sources, and size
 1453 distributions of submicron aerosols: Insights from the 2014 Nanjing Youth Olympic
 1454 Games, *Sci. Total Environ.*, 807, 150869,
 1455 <https://doi.org/10.1016/j.scitotenv.2021.150869>, 2022b.

1456 Wang, J. F., Ge, X. L., Chen, Y. F., Shen, Y. F., Zhang, Q., Sun, Y. L., Xu, J. Z., Ge,
 1457 S., Yu, H., and Chen, M. D.: Highly time-resolved urban aerosol characteristics during
 1458 springtime in Yangtze River Delta, China: insights from soot particle aerosol mass
 1459 spectrometry, *Atmos. Chem. Phys.*, 16, 9109-9127, [https://doi.org/10.5194/acp-16-](https://doi.org/10.5194/acp-16-9109-2016)
 1460 [9109-2016](https://doi.org/10.5194/acp-16-9109-2016), 2016.

1461 Wang, J. F., Ye, J. H., Zhang, Q., Zhao, J., Wu, Y. Z., Li, J. Y., Liu, D. T., Li, W. J.,
 1462 Zhang, Y. G., Wu, C., Xie, C. H., Qin, Y. M., Lei, Y. L., Huang, X. P., Guo, J. P., Liu, P.
 1463 F., Fu, P. Q., Li, Y. J., Lee, H. C., Choi, H., Zhang, J., Liao, H., Chen, M. D., Sun, Y. L.,
 1464 Ge, X. L., Martin, S. T., and Jacob, D. J.: Aqueous production of secondary organic
 1465 aerosol from fossil-fuel emissions in winter Beijing haze, *Proc. Natl. Acad. Sci. U. S.*
 1466 *A.*, 118, <https://doi.org/10.1073/pnas.2022179118>, 2021.
 1467 Wang, K., Zhang, Y., Huang, R. J., Cao, J. J., and Hoffmann, T.: UHPLC-Orbitrap
 1468 mass spectrometric characterization of organic aerosol from a central European city
 1469 (Mainz, Germany) and a Chinese megacity (Beijing), *Atmos. Environ.*, 189, 22-29,
 1470 <https://doi.org/10.1016/j.atmosenv.2018.06.036>, 2018a.
 1471 Wang, L. W., Wang, X. F., Gu, R. R., Wang, H., Yao, L., Wen, L., Zhu, F. P., Wang,
 1472 W. H., Xue, L. K., Yang, L. X., Lu, K. D., Chen, J. M., Wang, T., Zhang, Y. H., and
 1473 Wang, W. X.: Observations of fine particulate nitrated phenols in four sites in northern
 1474 China: concentrations, source apportionment, and secondary formation, *Atmos. Chem.*
 1475 *Phys.*, 18, 4349-4359, <https://doi.org/10.5194/acp-18-4349-2018>, 2018b.
 1476 Wang, Y., Huang, R. J., Zhong, H. B., Wang, T., Yang, L., Yuan, W., Xu, W., and
 1477 An, Z. S.: Predictions of the Optical Properties of Brown Carbon Aerosol by Machine
 1478 Learning with Typical Chromophores, *Environ. Sci. Technol.*, 58, 20588-20597,
 1479 <https://doi.org/10.1021/acs.est.4c09031>, 2024.
 1480 Wang, Y. J., Hu, M., Lin, P., Guo, Q. F., Wu, Z. J., Li, M. G., Zeng, L. M., Song,
 1481 Y., Zeng, L. W., Wu, Y. S., Guo, S., Huang, X. F., and He, L. Y.: Molecular
 1482 characterization of nitrogen-containing organic compounds in humic-like substances
 1483 emitted from straw residue burning, *Environ. Sci. Technol.*, 51, 5951-5961,
 1484 <https://doi.org/10.1021/acs.est.7b00248>, 2017.
 1485 Wang, Y. Q.: An open source software suite for multi-dimensional meteorological
 1486 data computation and visualisation, *Journal of Open Research Software*, 7,
 1487 <https://doi.org/10.5334/jors.267>, 2019.
 1488 Wen, H., Zhou, Y., Xu, X. Y., Wang, T. S., Chen, Q. L., Chen, Q. C., Li, W. J.,
 1489 Wang, Z., Huang, Z. W., Zhou, T., Shi, J. S., Bi, J. R., Ji, M. X., and Wang, X.: Water-

soluble brown carbon in atmospheric aerosols along the transport pathway of Asian dust: Optical properties, chemical compositions, and potential sources, *Sci. Total Environ.*, 789, 147971, <https://doi.org/10.1016/j.scitotenv.2021.147971>, 2021.

Wu, G. M., Ram, K., Fu, P. Q., Wang, W., Zhang, Y. L., Liu, X. Y., Stone, E. A., Pradhan, B. B., Dangol, P. M., Panday, A. K., Wan, X., Bai, Z. P., Kang, S. C., Zhang, Q. G., and Cong, Z. Y.: Water-soluble brown carbon in atmospheric aerosols from Godavari (Nepal), a regional representative of south Asia, *Environ. Sci. Technol.*, 53, 3471-3479, <https://doi.org/10.1021/acs.est.9b00596>, 2019a.

Wu, Y. Z., Ge, X. L., Wang, J. F., Shen, Y. F., Ye, Z. L., Ge, S., Wu, Y., Yu, H., and Chen, M. D.: Responses of secondary aerosols to relative humidity and photochemical activities in an industrialized environment during late winter, *Atmos. Environ.*, 193, 66-78, <https://doi.org/10.1016/j.atmosenv.2018.09.008>, 2018.

Wu, Y. Z., Liu, D. T., Wang, J. F., Shen, F. Z., Chen, Y. F., Cui, S. J., Ge, S., Wu, Y., Chen, M. D., and Ge, X. L.: Characterization of size-resolved hygroscopicity of black carbon-containing particle in urban environment, *Environ. Sci. Technol.*, 53, 14212-14221, <https://doi.org/10.1021/acs.est.9b05546>, 2019b.

Xian, J. K., Cui, S. J., Chen, X. Z., Wang, J. Y., Xiong, Y. F., Gu, C. J., Wang, Y., Zhang, Y. J., Li, H. W., Wang, J. F., and Ge, X. L.: Online chemical characterization of atmospheric fine secondary aerosols and organic nitrates in summer Nanjing, China, *Atmos. Res.*, 290, 106783, <https://doi.org/10.1016/j.atmosres.2023.106783>, 2023.

Xie, M. J., Mladenov, N., Williams, M. W., Neff, J. C., Wasswa, J., and Hannigan, M. P.: Water soluble organic aerosols in the Colorado Rocky Mountains, USA: composition, sources and optical properties, *Sci. Rep.*, 6, 39339, <https://doi.org/10.1038/srep39339>, 2016.

Xie, X. C., Chen, Y. F., Nie, D. Y., Liu, Y., Liu, Y., Lei, R. Y., Zhao, X. Y., Li, H. W., and Ge, X. L.: Light-absorbing and fluorescent properties of atmospheric brown carbon: A case study in Nanjing, China, *Chemosphere*, 251, 126350, <https://doi.org/10.1016/j.chemosphere.2020.126350>, 2020.

Xing, C., Wan, Y. B., Wang, Q. Q., Kong, S. F., Huang, X. P., Ge, X. L., Xie, M.

1519 J., and Yu, H.: Molecular Characterization of Brown Carbon Chromophores in
1520 Atmospherically Relevant Samples and Their Gas-Particle Distribution and Diurnal
1521 Variation in the Atmosphere, *J. Geophys. Res.: Atmos.*, 128, e2022JD038142,
1522 <https://doi.org/10.1029/2022JD038142>, 2023.

1523 Xu, L. L., Lin, G. X., Liu, X. H., Wu, C. L., Wu, Y. F., and Lou, S. J.: Constraining
1524 Light Absorption of Brown Carbon in China and Implications for Aerosol Direct
1525 Radiative Effect, *Geophys. Res. Lett.*, 51, <https://doi.org/10.1029/2024gl109861>, 2024.

1526 Yan, G. and Kim, G.: Speciation and sources of brown carbon in precipitation at
1527 seoul, Korea: insights from excitation–emission matrix spectroscopy and carbon
1528 isotopic analysis, *Environ. Sci. Technol.*, 51, 11580-11587,
1529 <https://doi.org/10.1021/acs.est.7b02892>, 2017.

1530 Yan, J. P., Wang, X. P., Gong, P., Wang, C. F., and Cong, Z. Y.: Review of brown
1531 carbon aerosols: recent progress and perspectives, *Sci. Total Environ.*, 634, 1475-1485,
1532 <https://doi.org/10.1016/j.scitotenv.2018.04.083>, 2018.

1533 Yassine, M. M., Harir, M., Dabek-Z., E., and Schmitt-K., P.: Structural
1534 characterization of organic aerosol using Fourier transform ion cyclotron resonance
1535 mass spectrometry: Aromaticity equivalent approach, *Rapid Commun. Mass Spectrom.*,
1536 28, 2445-2454, <https://doi.org/doi.org/10.1002/rcm.7038>, 2014.

1537 Ye, Z. L., Qu, Z. X., Ma, S. S., Luo, S. P., Chen, Y. T., Chen, H., Chen, Y. F., Zhao,
1538 Z. Z., Chen, M. D., and Ge, X. L.: A comprehensive investigation of aqueous-phase
1539 photochemical oxidation of 4-ethylphenol, *Sci. Total Environ.*, 685, 976-985,
1540 <https://doi.org/10.1016/j.scitotenv.2019.06.276>, 2019.

1541 Ye, Z. L., Li, Q., Liu, J. S., Luo, S. P., Zhou, Q. F., Bi, C. L., Ma, S. S., Chen, Y.
1542 F., Chen, H., Li, L., and Ge, X. L.: Investigation of submicron aerosol characteristics in
1543 Changzhou, China: Composition, source, and comparison with co-collected PM_{2.5},
1544 *Chemosphere*, 183, 176-185, <https://doi.org/10.1016/j.chemosphere.2017.05.094>, 2017.

1545 Yu, H. R., Liang, H., Qu, F. S., Han, Z. S., Shao, S. L., Chang, H. Q., and Li, G.
1546 B.: Impact of dataset diversity on accuracy and sensitivity of parallel factor analysis
1547 model of dissolved organic matter fluorescence excitation-emission matrix, *Sci. Rep.*,

1548 5, 10207, <https://doi.org/10.1038/srep10207>, 2015.

1549 Yu, J. T., Yan, C. Q., Liu, Y., Li, X. Y., Zhou, T., and Zheng, M.: Potassium: a tracer
 1550 for biomass burning in Beijing?, *Aerosol Air Qual. Res.*, 18, 2447-2459,
 1551 <https://doi.org/10.4209/aaqr.2017.11.0536>, 2018.

1552 Zhang, B. Q., Zhang, Y. J., Zhang, K. X., Zhang, Y. C., Ji, Y., Zhu, B. Z., Liang, Z.
 1553 Y., Wang, H. L., and Ge, X. L.: Machine learning assesses drivers of PM_{2.5} air pollution
 1554 trend in the Tibetan Plateau from 2015 to 2022, *Sci. Total Environ.*, 878, 163189,
 1555 <https://doi.org/10.1016/j.scitotenv.2023.163189>, 2023.

1556 Zhang, Q., Jimenez, J. L., Canagaratna, M. R., Ulbrich, I. M., Ng, N. L., Worsnop,
 1557 D. s. R., and Sun, Y. L.: Understanding atmospheric organic aerosols via factor analysis
 1558 of aerosol mass spectrometry: a review, *Anal. Bioanal. Chem.*, 401, 3045-3067,
 1559 <https://doi.org/10.1007/s00216-011-5355-y>, 2011.

1560 Zhang, S. Y.: Detection of scopolamine in nori fruit juice and its traditional chinese
 1561 medicine compound health products by high performance liquid chromatography,
 1562 *World Latest Medicine Information*, 18, 91-92, [https://doi.org/10.19613/j.cnki.1671-](https://doi.org/10.19613/j.cnki.1671-3141.2018.82.066)
 1563 [3141.2018.82.066](https://doi.org/10.19613/j.cnki.1671-3141.2018.82.066), 2018.

1564 Zhang, X. L., Lin, Y. H., Surratt, J. D., and Weber, R. J.: Sources, composition and
 1565 absorption Ångström exponent of light-absorbing organic components in aerosol
 1566 extracts from the Los Angeles basin, *Environ. Sci. Technol.*, 47, 3685-3693,
 1567 <https://doi.org/10.1021/es305047b>, 2013.

1568 Zhang, Y. Z., Forrister, H., Liu, J. M., Dibb, J., Anderson, B., Schwarz, J. P.,
 1569 Perring, A. E., Jimenez, J. L., Campuzano-Jost, P., Wang, Y. H., Nenes, A., and Weber,
 1570 R. J.: Top-of-atmosphere radiative forcing affected by brown carbon in the upper
 1571 troposphere, *Nat. Geosci.*, 10, 486-489, <https://doi.org/10.1038/ngeo2960>, 2017.

1572 Zhao, R., Lee, A. K. Y., Huang, L., Li, X., Yang, F., and Abbatt, J. P. D.:
 1573 Photochemical processing of aqueous atmospheric brown carbon, *Atmos. Chem. Phys.*,
 1574 15, 6087-6100, <https://doi.org/10.5194/acp-15-6087-2015>, 2015.

1575 Zhong, M., Xu, J. Z., Wang, H. Q., Gao, L., Zhu, H. X., Zhai, L. X., Zhang, X. H.,
 1576 and Zhao, W. H.: Characterizing water-soluble brown carbon in fine particles in four

1577 typical cities in northwestern China during wintertime: integrating optical properties
 1578 with chemical processes, *Atmos. Chem. Phys.*, 23, 12609-12630,
 1579 <https://doi.org/10.5194/acp-23-12609-2023>, 2023.
 1580 Zhu, B., Fang, J., Zhang, Y., Qiu, J., Chen, K., Zhang, K., Liang, H., Yang, H.,
 1581 Ding, Y., and Ge, X.: Machine learning elucidates ubiquity of enhanced ozone air
 1582 pollution in China linked to the spring festival effect, *Atmos. Pollut. Res.*, 15, 102127,
 1583 <https://doi.org/10.1016/j.apr.2024.102127>, 2024.
 1584 Zorn, S. R., Drewnick, F., Schott, M., Hoffmann, T., and Borrmann, S.:
 1585 Characterization of the South Atlantic marine boundary layer aerosol using an aerodyne
 1586 aerosol mass spectrometer, *Atmos. Chem. Phys.*, 8, 4711-4728,
 1587 <https://doi.org/10.5194/acp-8-4711-2008>, 2008.
 1588 Zsolnay, A., Baigar, E., Jimenez, M., Steinweg, B., and Saccomandi, F.:
 1589 Differentiating with fluorescence spectroscopy the sources of dissolved organic matter
 1590 in soils subjected to drying, *Chemosphere*, 38, 45-50, [https://doi.org/10.1016/S0045-](https://doi.org/10.1016/S0045-6535(98)00166-0)
 1591 [6535\(98\)00166-0](https://doi.org/10.1016/S0045-6535(98)00166-0), 1999.
 1592

1593 Table 1. The average mass concentrations of major chemical components as well as the
1594 parameters of optical properties of PM_{2.5} collected in Nanjing during two seasons.

	Summer Season (SS)			Cold Season (CS)		
	Daytime	Nighttime	Average	Daytime	Nighttime	Average
OC ($\mu\text{g m}^{-3}$)	7.02 \pm 3.04	6.87 \pm 2.51	6.94 \pm 2.76	12.9 \pm 5.77	12.74 \pm 5.29	12.82 \pm 5.51
EC ($\mu\text{g m}^{-3}$)	1.13 \pm 0.31	1.22 \pm 0.37	1.17 \pm 0.34	1.94 \pm 0.93	1.6 \pm 0.74	1.77 \pm 0.86
AAE _{WSOC}	6.34 \pm 0.65	6.35 \pm 0.69	6.35 \pm 0.67	6.43 \pm 0.68	6.44 \pm 0.86	6.43 \pm 0.77
AAE _{MSOC}	6.02 \pm 0.90	5.96 \pm 0.96	5.99 \pm 0.92	7.06 \pm 0.94	6.70 \pm 0.65	6.89 \pm 0.82
WSOC ($\mu\text{g m}^{-3}$)	4.06 \pm 1.31	4.45 \pm 1.44	4.26 \pm 1.38	5.81 \pm 2.29	5.75 \pm 2.25	6.34 \pm 2.27
MSOC ($\mu\text{g m}^{-3}$)	5.64 \pm 2.12	5.79 \pm 1.89	5.72 \pm 1.99	10.42 \pm 4.98	10.49 \pm 4.57	10.45 \pm 4.75
Total ions ($\mu\text{g m}^{-3}$)	18.00 \pm 5.49	18.69 \pm 8.05	18.49 \pm 6.91	35.41 \pm 15.02	43.12 \pm 17.94	39.22 \pm 16.88
Abs _{365, WSOC} (M m ⁻¹)	2.15 \pm 0.90	2.38 \pm 0.80	2.27 \pm 0.85	4.89 \pm 2.63	4.86 \pm 2.46	4.87 \pm 2.53
Abs _{365, MSOC} (M m ⁻¹)	3.44 \pm 1.40	3.82 \pm 1.55	3.64 \pm 1.48	4.65 \pm 2.24	5.31 \pm 2.71	4.97 \pm 2.49
MAE _{365, WSOC} (m ² g ⁻¹)	0.54 \pm 0.16	0.56 \pm 0.15	0.55 \pm 0.16	0.73 \pm 0.20	0.77 \pm 0.21	0.75 \pm 0.21
MAE _{365, MSOC} (m ² g ⁻¹)	0.68 \pm 0.32	0.75 \pm 0.30	0.72 \pm 0.31	0.48 \pm 0.18	0.52 \pm 0.16	0.50 \pm 0.17
SFE _{WSOC} (W g ⁻¹)	2.16 \pm 1.29	2.24 \pm 1.36	2.20 \pm 1.33	3.16 \pm 1.8	3.42 \pm 1.25	3.24 \pm 1.84
SFE _{MSOC} (W g ⁻¹)	2.28 \pm 2.37	2.55 \pm 1.85	2.43 \pm 2.10	2.19 \pm 1.01	2.26 \pm 0.81	2.23 \pm 0.91

1595

1596 Table 2. Multi-linear regression results of the four factors and corresponding average
 1597 contributions to the total light absorption of water-soluble organics (WSOA).

Factor	Regression Coefficient($\text{m}^2 \cdot \text{g}^{-1}$)		Contribution (%)
	Average	Standard Error	
HOA	0.71	0.11	33.05
BBOA	0.71	0.06	15.49
OOA1	0.12	0.07	6.00
OOA2	0.83	0.14	45.46

1598

1599 Table 3. The average values of fluorescence indices of both water-soluble organic
1600 carbon (WSOC) and methanol-soluble organic carbon (MSOC).

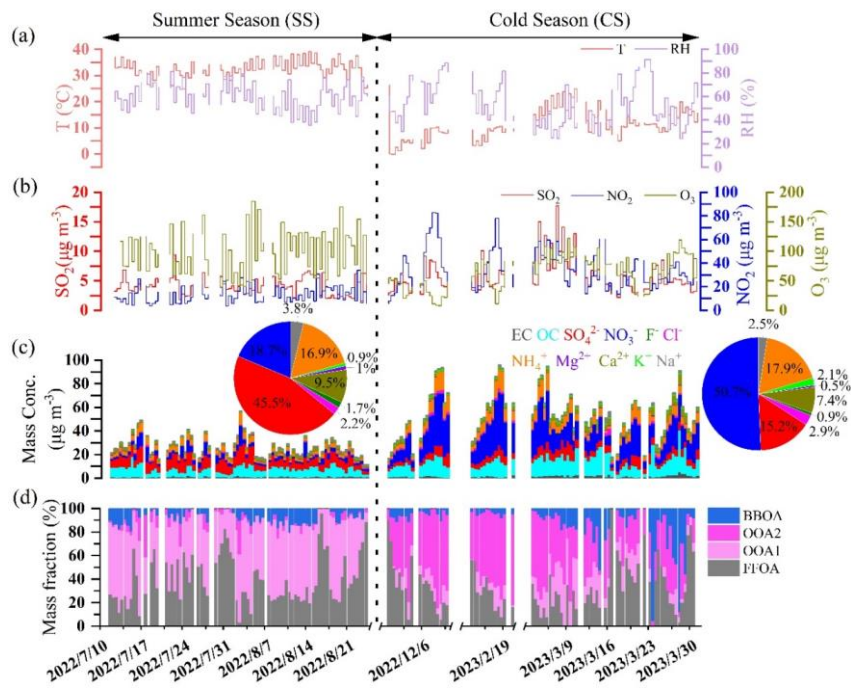
	Summer Season (SS)			Cold Season (CS)		
	Day	Night	Average	Day	Night	Average
HIX _{WSOC}	3.16±0.74	3.51±1.12	3.34±0.97	4.68±0.94	4.67±0.91	4.68±0.92
HIX _{MSOC}	2.65±0.99	2.78±0.86	2.72±0.92	3.42±0.73	3.53±0.58	3.48±0.66
FI _{WSOC}	1.85±0.16	1.97±0.17	1.91±0.18	1.89±0.11	1.92±0.09	1.90±0.10
FI _{MSOC}	2.25±0.26	2.30±0.31	2.27±0.28	2.10±0.15	2.12±0.14	2.11±0.15
BIX _{WSOC}	0.81±0.16	0.86±0.14	0.84±0.15	0.86±0.10	0.91±0.08	0.88±0.09
BIX _{MSOC}	0.89±0.19	0.9±0.13	0.90±0.16	0.95±0.10	0.97±0.11	0.96±0.10

1601

1602 Table 4. The number percentages of organosulfates (OSs) in CHOS compounds in ESI⁻
 1603 mode and those of nitrooxy-OSs in CHONS compounds in both modes.

	SS		CS	
	Daytime	Nighttime	Daytime	Nighttime
OSs (ESI ⁻)	34.8%	42.3%	54.3%	68.6%
Nitrooxy-OSs (ESI ⁻)	5.3%	12.0%	11.0%	12.5%
Nitrooxy-OSs (ESI ⁺)	10.3%	11.8%	10.5%	9.8%

1604



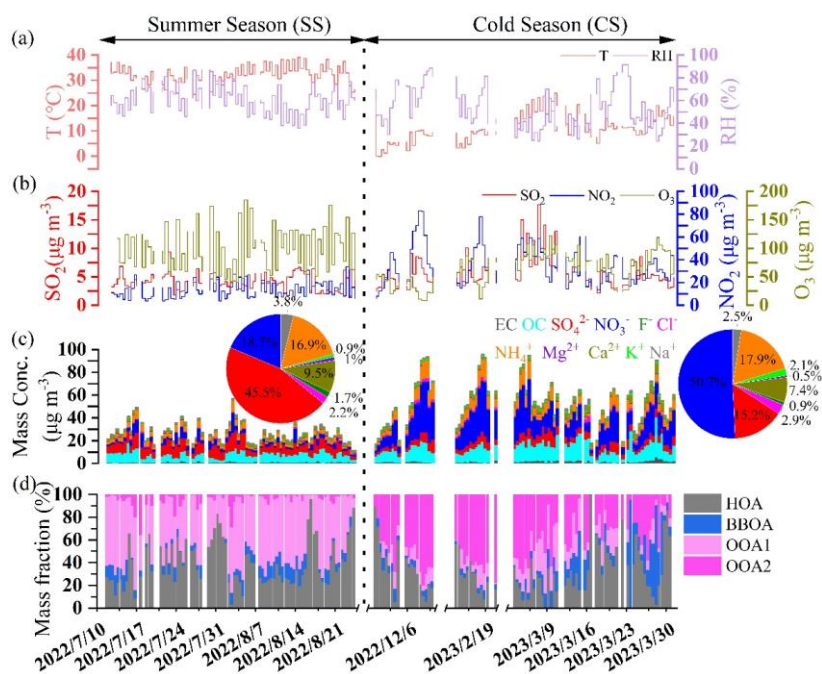
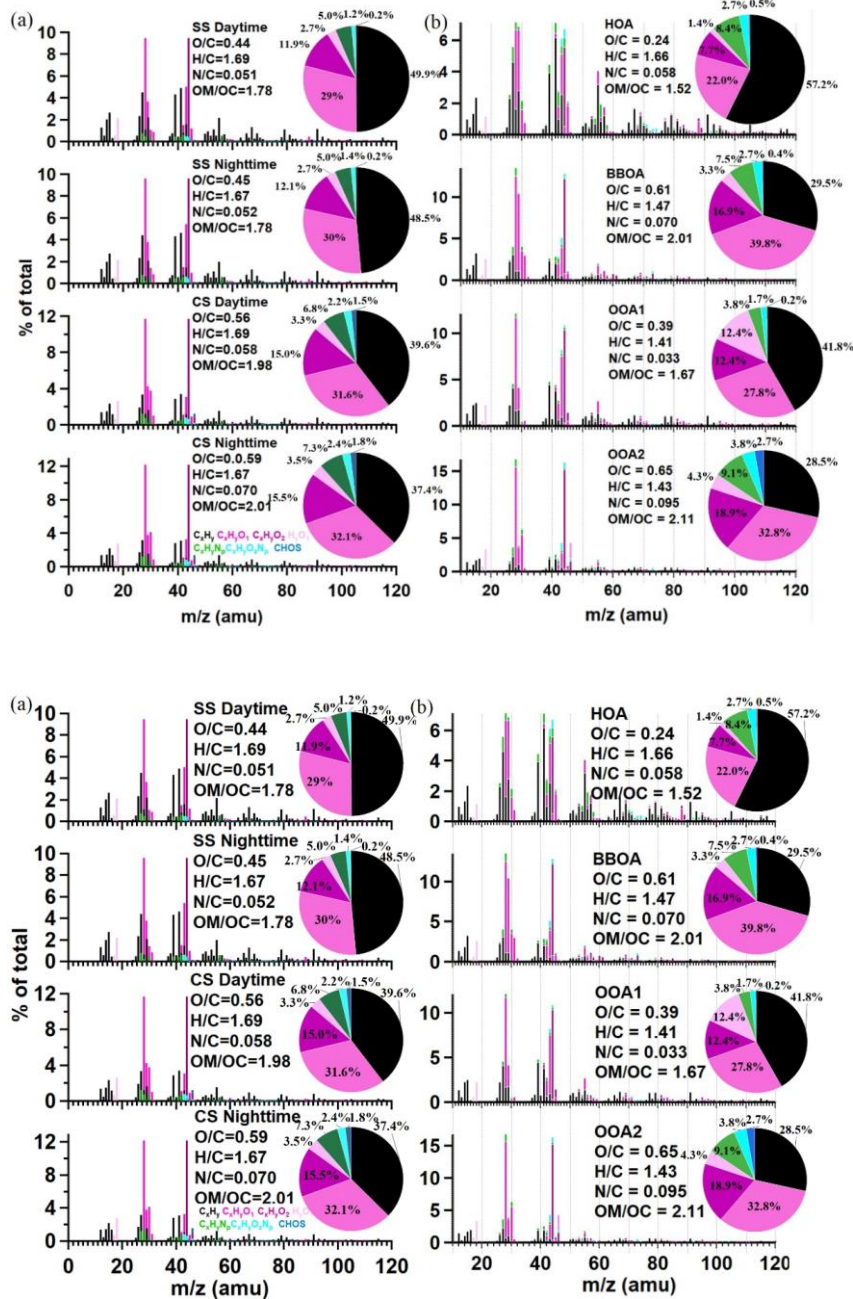


Figure 1. Time series of: (a) air temperature (T) and relative humidity (RH); (b) concentrations of nitrogen dioxide (NO₂), sulfur dioxide (SO₂) and ozone (O₃); (c) concentrations of different inorganic ions, total organic carbon (OC), and elemental carbon (EC) (two inset pies are the average mass contributions of difference ions to the total ions during SS and CS, respectively); and (d) mass percentages of different factors with respect to the total water-soluble OA



1619 OOA2). Ions are classified into and colored by different ion families, and inset pies in
1620 both charts show the mass fractional contributions of different ion families to the total
1621 HRMS correspondingly.
1622

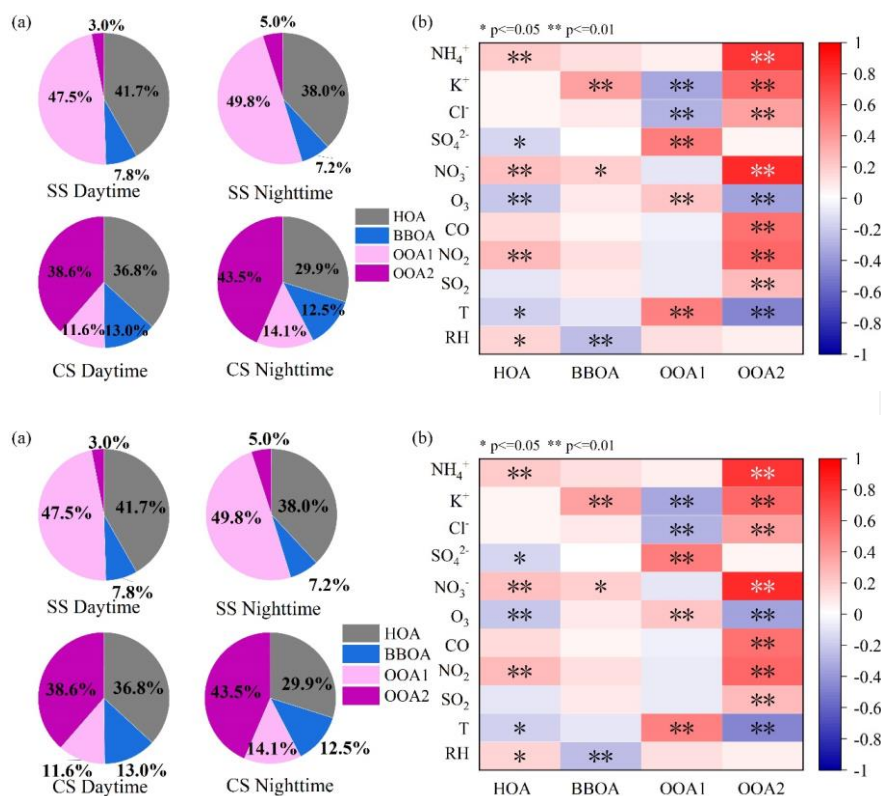


Figure 3. (a) Average mass contributions of the four factor to WSOA during different periods, and (b) cross-correlation coefficients (Pearson's r) among the four factors and other aerosol components as well as gaseous species.

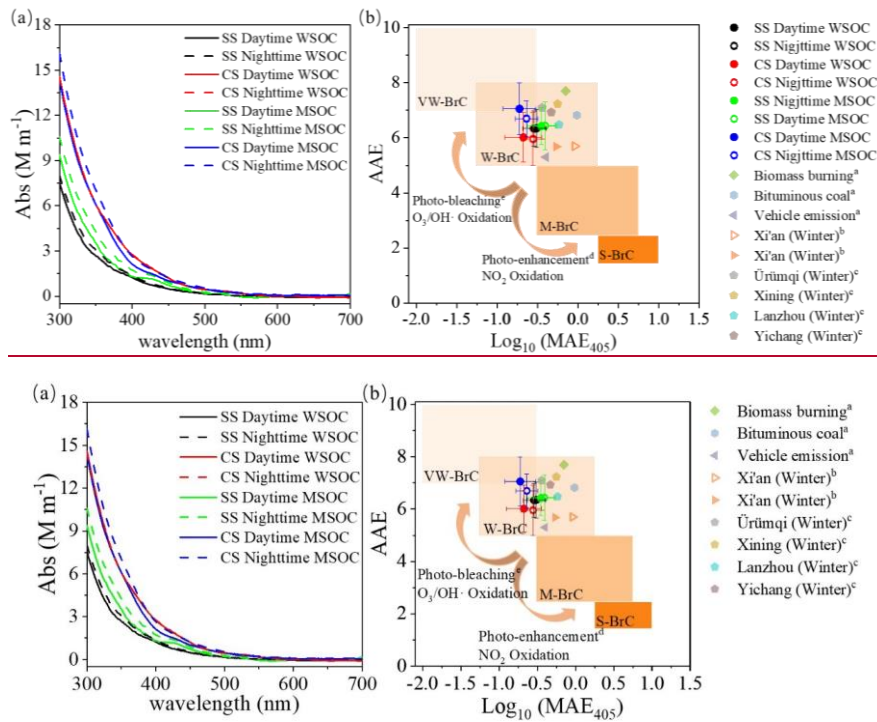


Figure 4. (a) Light absorption coefficients (Abs) of the water-soluble OC (WSOC) and methanol-soluble OC (MSOC) as a function of wavelength, and (b) distribution of the measured data in the $\log_{10}(MAE_{405})$ -AAE space (Saleh, 2020) (MAE_{405} : Mass absorption efficiency at 405 nm; AAE: Absorption Ångström Exponent; The shaded areas indicate very weakly (VW), weakly (W), moderately (M), and strongly (S) absorbing brown carbon (BrC), respectively; Other markers indicate results from ^a Huang et al. (2018), ^b Chen et al. (2018) and ^c Zhong et al. (2023).

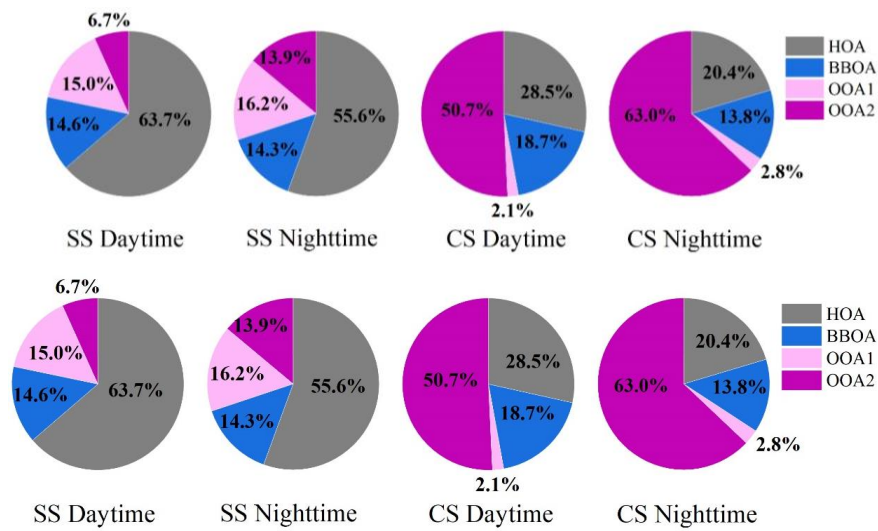
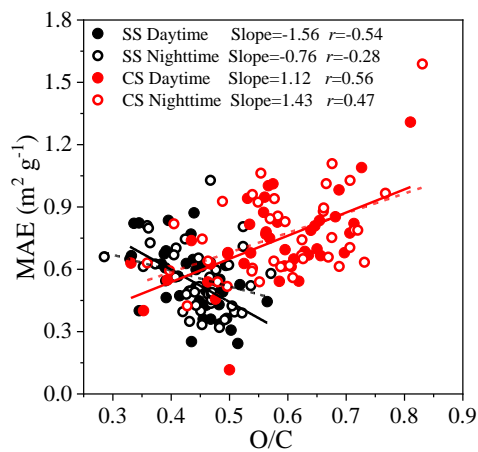


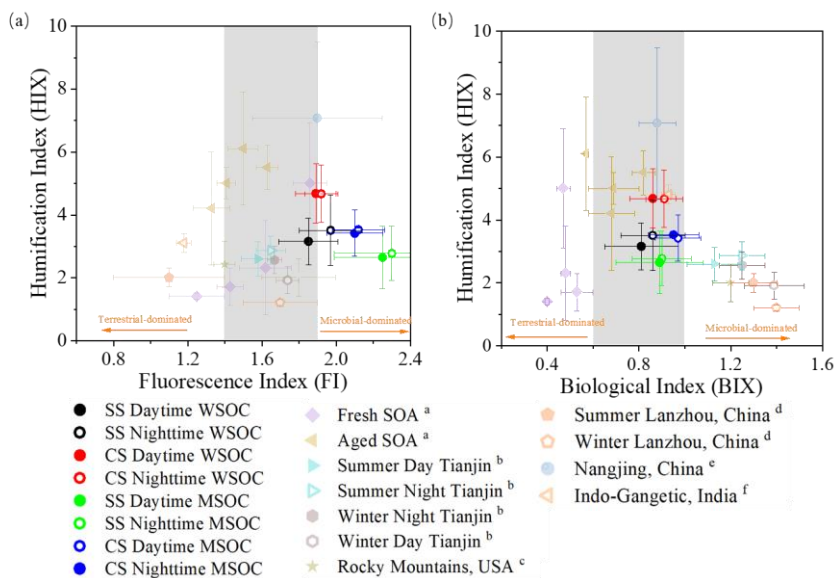
Figure 5. Contributions of the four factors to the total light absorption of WSOA during different periods.



1644

1645 Figure 6. Scatter plot of MAE₃₆₅ (mass absorption efficiency at 365 nm) versus the

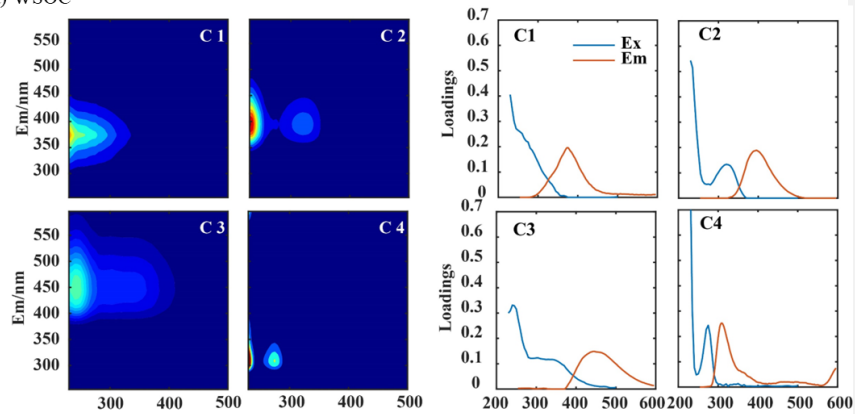
1646 oxygen-to-carbon (O/C) ratios for the WSOA.



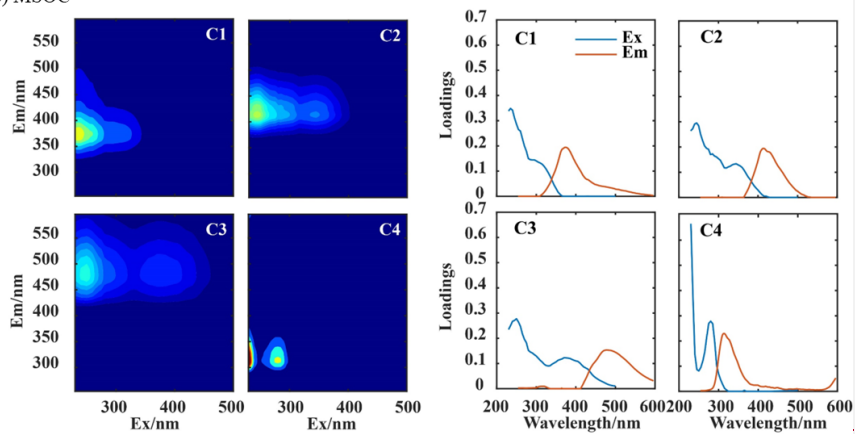
1647

1648 Figure 7. Distribution of the fluorescent indices of measured data in this study and a
 1649 few other studies (^a Lee et al. (2013), ^b Deng et al. (2022), ^c Xie et al. (2016), ^d Qin et
 1650 al. (2018), ^e Xie et al. (2016), ^f Dey et al. (2021)): (a) Humidication index (HIX) versus
 1651 fluorescenc index (FI), and (b) HIX versus biological index (BIX). The shaded areas
 1652 marked 0.6 ~ 1 of BIX (Huguet et al., 2009) and 1.6 ~ 1.9 of FI (Mcknight et al., 2001).
 1653

(a) WSOC



(b) MSOC



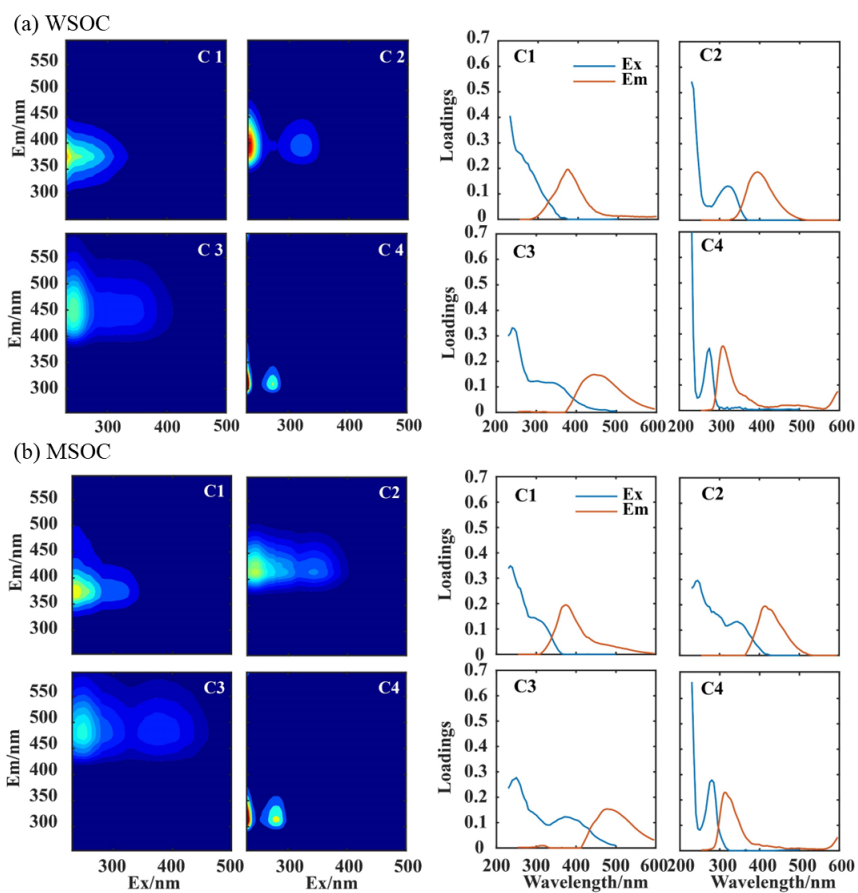


Figure 8. Four fluorescence components (C1 ~ C4) and the corresponding fluorescent intensities of emission (brown) and excitation (blue) against wavelength: (a) WSOC, and (b) MSOC.

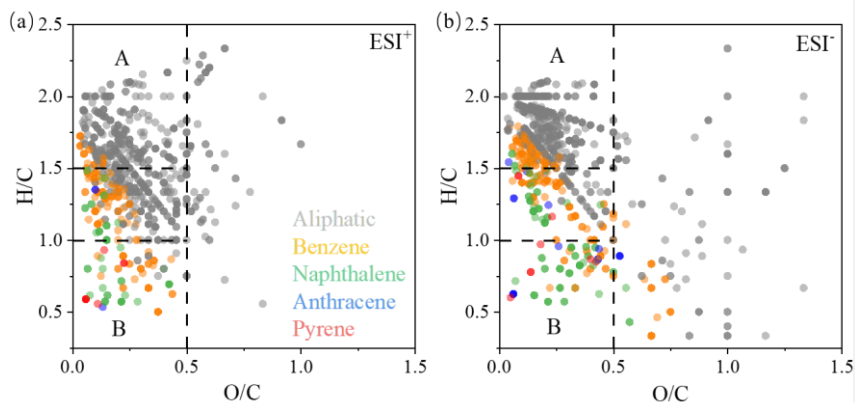
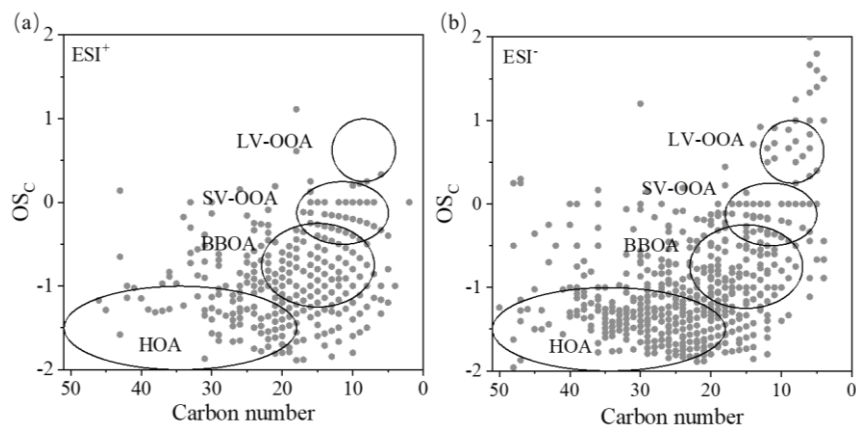
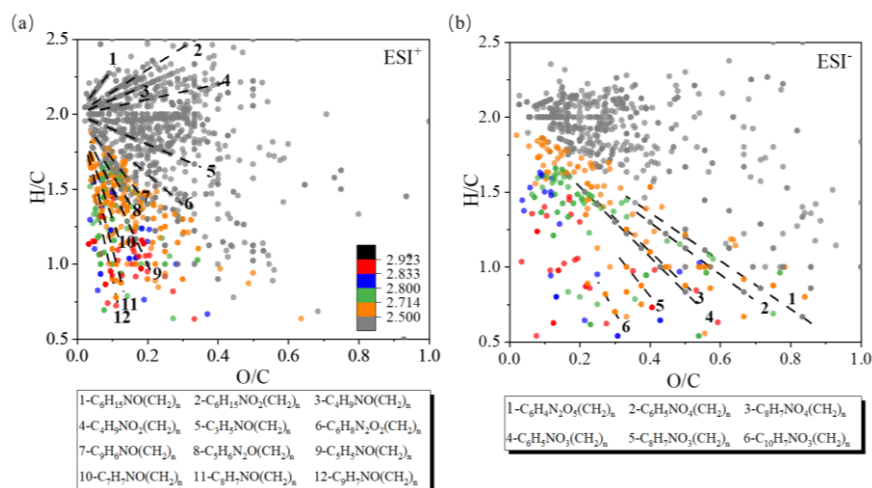


Figure 9. Van Krevelen diagram for CHO compounds detected in (a) ESI⁺ and (b) ESI⁻ mode. The markers with different colors represent aliphatic compounds ($X_c < 2.50$), aromatic benzene ring structures ($2.50 \leq X_c < 2.71$), naphthalene ring structures ($2.71 \leq X_c < 2.80$), anthracene ring structures ($2.80 \leq X_c < 2.83$), and pyrene ring structures ($2.83 \leq X_c < 2.92$), respectively (Mao et al., 2022).

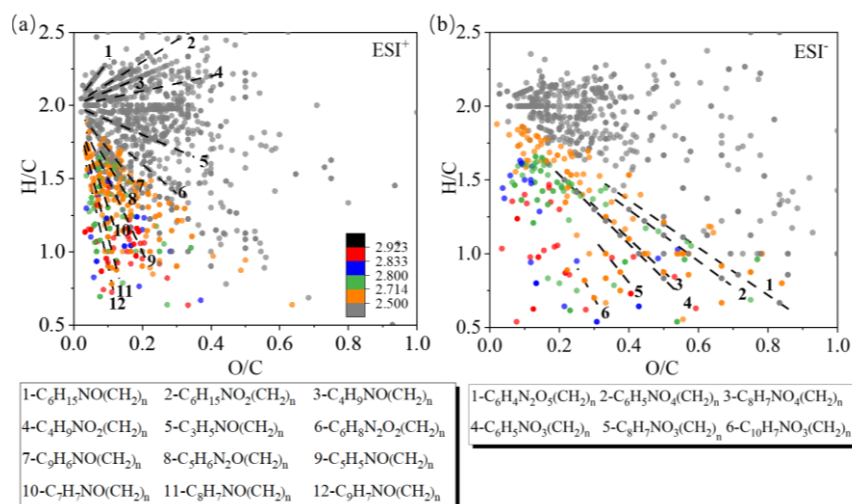


1669
 1670 Figure 10. Scatter plots of carbon oxidation state (OS_c) versus carbon number for CHO
 1671 compounds: (a) ESI⁺ mode, and (b) ESI⁻ mode. The circled areas represent those from
 1672 fossil fuel combustion hydrocarbon-like OA (HOA), biomass burning OA (BBOA),
 1673 semi-volatile oxygenated OA (SV-OOA) and low-volatility oxygenated OA (LV-
 1674 OOA)(Kroll et al., 2011).
 1675

1676



1677

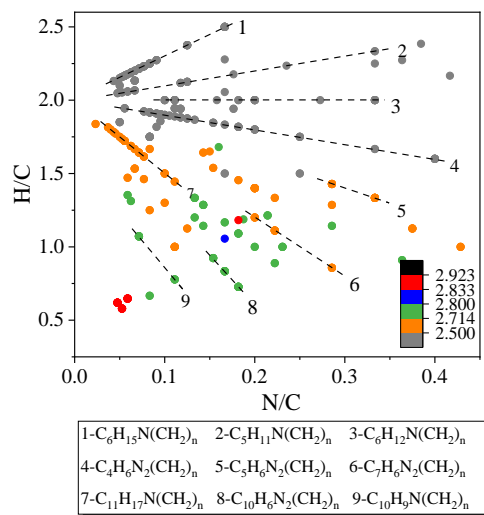


1678

1679

1680 Figure 11. Van Krevelen diagram for CHON compounds detected in both ESI⁺ and ESI⁻
 1681 mode. The data are also colored by Xc values (See caption of Fig. 9), and the different
 1682 dash lines represent different series of compounds.
 1683

1684



1685

1686

1687 Figure 12. Van Krevelen diagram of the CHN compounds in ESI⁺ mode. The data are
 1688 also colored by Xc values (See caption of Fig. 9), and the different dash lines represent
 1689 different series of compounds.

1690

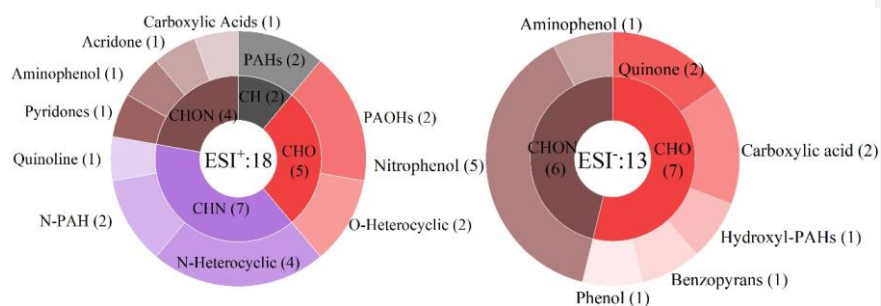


Figure 13. Distributions of the machine learning identified key light absorbing organic compounds (details in Table S2 in the supplement)